

DDC FILE COPY 1

REPORT DOCUMENTATION PAGE		READ INSTRUCTIONS BEFORE COMPLETING FORM
1. REPORT NUMBER AFIT/CI/NR 88- 44	2. GOVT ACCESSION NO.	3. RECIPIENT'S CATALOG NUMBER
4. TITLE (and Subtitle) THE EFFECTS OF INCOMING BOUNDARY LAYER THICKNESS ON UNSTEADY SHOCK-INDUCED TURBULENT SEPARATIONS INDUCED BY CYLINDERS		5. TYPE OF REPORT & PERIOD COVERED MS THESIS
		6. PERFORMING ORG. REPORT NUMBER
7. AUTHOR(s) DOUGLAS ROBERT SMITH		8. CONTRACT OR GRANT NUMBER(s)
PERFORMING ORGANIZATION NAME AND ADDRESS AFIT STUDENT AT: UNIVERSITY OF TEXAS - AUSTIN		10. PROGRAM ELEMENT, PROJECT, TASK AREA & WORK UNIT NUMBERS
9. CONTROLLING OFFICE NAME AND ADDRESS		12. REPORT DATE 1988
		13. NUMBER OF PAGES 105
14. MONITORING AGENCY NAME & ADDRESS (if different from Controlling Office) AFIT/NR Wright-Patterson AFB OH 45433-6583		15. SECURITY CLASS. (of this report) UNCLASSIFIED
		15a. DECLASSIFICATION/DOWNGRADING SCHEDULE
16. DISTRIBUTION STATEMENT (of this Report) DISTRIBUTED UNLIMITED: APPROVED FOR PUBLIC RELEASE		
17. DISTRIBUTION STATEMENT (of the abstract entered in Block 20, if different from Report) SAME AS REPORT		
18. SUPPLEMENTARY NOTES Approved for Public Release: IAW AFR 190-1 LYNN E. WOLAVER <i>Lynn Wolaver</i> 18 July 88 Dean for Research and Professional Development Air Force Institute of Technology Wright-Patterson AFB OH 45433-6583		
19. KEY WORDS (Continue on reverse side if necessary and identify by block number)		
20. ABSTRACT (Continue on reverse side if necessary and identify by block number) ATTACHED		

AD-A196 190

DTIC
ELECTE
AUG 6 4 1988
S D
CD

ABSTRACT

Wall pressure fluctuations have been measured under the unsteady separation shock/turbulent boundary layer interaction induced by unswept circular cylinders to determine the role of the incoming turbulent boundary layer thickness on the shock motion. Measurements were taken in a high Reynolds number, Mach 5 flow in the turbulent boundary layer developed on the tunnel floor. The wall temperature was adiabatic. High frequency response, miniature pressure transducers were mounted flush with the tunnel floor to measure the pressure fluctuations caused by the shock motion. A conditional sampling algorithm was used to separate the pressure fluctuations due to the shock motion, from those fluctuations associated with the incoming and downstream turbulent boundary layer. Standard time series analysis techniques were used to analyze the data. The results show that the turbulent boundary layer has only second order effects on the frequency of the separation shock. Shock frequencies are at least one order of magnitude less than the large eddy frequency of the turbulent boundary layer. The low frequency pressure fluctuations of the separated region are within the same frequency range as the shock frequencies. These pressure fluctuations are a possible cause of the shock motion and warrant further investigation.

THE EFFECTS OF INCOMING BOUNDARY LAYER
THICKNESS ON UNSTEADY SHOCK-INDUCED
TURBULENT SEPARATIONS INDUCED
BY CYLINDERS

APPROVED:

D S Dolly
Parker Lab



Accession For	
NTIS CRA&I	<input checked="" type="checkbox"/>
DTIC TAB	<input type="checkbox"/>
Unannounced Justification	<input type="checkbox"/>
By	
Date	
Distribution	
A-1	

To my wonderful wife Kim.
I could not have done this without you.

**THE EFFECTS OF INCOMING BOUNDARY LAYER
THICKNESS ON UNSTEADY SHOCK-INDUCED
TURBULENT SEPARATIONS INDUCED
BY CYLINDERS**

by

DOUGLAS ROBERT SMITH, B.S.

THESIS

Presented to the Faculty of the Graduate School of
The University of Texas at Austin
in Partial Fulfillment
of the Requirements
for the Degree of

MASTER OF SCIENCE IN ENGINEERING

THE UNIVERSITY OF TEXAS AT AUSTIN

December, 1987

ACKNOWLEDGEMENTS

The author wishes to thank Professor David S. Dolling for his guidance, advice, and patience during this work. Special thanks is given to Eddie Zihlman, and Frank Wise for their technical expertise. The invaluable assistance of Rich Gramann is also acknowledged.

November 1987

ABSTRACT

Wall pressure fluctuations have been measured under the unsteady separation shock/turbulent boundary layer interaction induced by unswept circular cylinders to determine the role of the incoming turbulent boundary layer thickness on the shock motion. Measurements were taken in a high Reynolds number, Mach 5 flow in the turbulent boundary layer developed on the tunnel floor. The wall temperature was adiabatic. High frequency response, miniature pressure transducers were mounted flush with the tunnel floor to measure the pressure fluctuations caused by the shock motion. A conditional sampling algorithm was used to separate the pressure fluctuations due to the shock motion, from those fluctuations associated with the incoming and downstream turbulent boundary layer. Standard time series analysis techniques were used to analyze the data. The results show that the turbulent boundary layer has only second order effects on the frequency of the separation shock. Shock frequencies are at least one order of magnitude less than the large eddy frequency of the turbulent boundary layer. The low frequency pressure fluctuations of the separated region are within the same frequency range as the shock frequencies. These pressure fluctuations are a possible cause of the shock motion and warrant further investigation.

TABLE OF CONTENTS

Section		Page
	List of Figures	viii
	List of Tables	x
	Nomenclature	xi
1	INTRODUCTION	1
1.1	Background	1
1.2	Recent Studies	3
1.3	Objective of Current Study	5
2	LITERATURE REVIEW	6
2.1	Background	6
2.1.1	Early Research	6
2.1.2	General Flow Characteristics	8
2.2	Shock Motion/Dynamics	9
2.3	Recent Research	10
2.3.1	Blunt Fin Results	11
2.3.2	Compression Ramp Studies	13
2.3.3	Cylinder Results	21
2.3.4	Additional Studies/Analyses	23
2.4	Summary	26
3	EXPERIMENTAL PROGRAM	28
3.1	Test Facility	28
3.2	Incoming Flow Conditions	28
3.3	Model	29
3.4	Pressure Transducers	30
3.4.1	Specifications	30
3.4.2	Calibration of Transducers	32
3.5	Additional Instrumentation	33

3.6	Test Procedure	34
3.6.1	Separation Location	34
3.6.2	Electronic Noise Estimation and Reduction	35
3.6.3	Boundary Layer Analysis	36
3.6.4	Intermittent Region	36
4	RESULTS AND DISCUSSION	37
4.1	Overview	37
4.2	Incoming Flow Analysis	38
4.2.1	Boundary Layer Analysis	38
4.2.2	Flow Visualization Results	40
4.3	Intermittent Region Analysis	42
4.3.1	Flow Characteristics	42
4.3.2	Probability Distributions of Pressure Fluctuation Amplitudes	44
4.3.3	Power Spectral Density Plots	46
4.3.3.1	Evolution of the Power Spectra at Different Intermittencies	46
4.3.3.2	Power Spectral Density Plots at $\gamma \approx .50$	50
4.3.4	Zero Crossing Frequencies	50
4.3.5	Probability Distributions of the Shock Periods	51
4.3.6	Probability Distributions of the Shock Frequency	53
4.3.7	Calculation of Shock Speeds	54
4.4	Implications of Results	55
5	CONCLUSIONS	57
6	Appendix	60
6.1	Threshold Sensitivity Study	60
	Tables	63
	Figures	65
	References	101
	Vita	

LIST OF FIGURES

Figure	Description	Page
1	Pressure Fluctuations in Front of a Forward Facing Step	65
2	Distribution of P_w and σ_{P_w} in Compression Ramp Flowfield	66
3	Distribution of P_w and σ_{P_w} in Blunt Fin Flowfield	67
4	Conversion of Pressure Signal into Box-Car Function	68
5	Test Configuration	69
6	Instrumentation Block Diagram	70
7	Typical Flow Visualization Pattern	71
8	Mean Velocity Profiles in Wall Coordinates	72
9	Mean Velocity Profiles (Y/δ_o vs U/U_∞)	73
10	Power Spectra of the Boundary Layer P_w Fluctuation Amplitudes	74
11	Power Spectra of the Boundary Layer P_w Fluctuation Amplitudes ($f_{\text{cutoff}} = 100$ kHz)	75
12	Probability Distribution of the P_w Fluctuation Amplitudes	76
13	Streamwise Distribution of P_w	77
14	Streamwise Distribution of σ_{P_w}	78
15	Distribution of σ_{P_w} Through Intermittent Region	79
16	Streamwise Distribution of Flatness Coefficient	80
17	Streamwise Distribution of Skewness Coefficient	81
18	Streamwise Distribution of Intermittency	82
19	a. Pressure-Time History ($\gamma \approx .30$), b. Probability Distribution of P_w Fluctuation Amplitudes ($\gamma \approx .30$)	83
20	a. Pressure-Time History ($\gamma \approx .70$), b. Probability Distribution of P_w Fluctuation Amplitudes ($\gamma \approx .70$)	84

21	Dimensional Power Spectra of the P_w Fluctuation Amplitudes (TF, 1.91 cm Cyl)	85
22	Normalized Power Spectra of the P_w Fluctuation Amplitudes (TF, 1.91 cm Cyl)	86
23	Normalized Power Spectra of the P_w Fluctuation Amplitudes (TF, 1.91 cm Cyl)	87
24	Dimensional Power Spectra of the P_w Fluctuation Amplitudes (FP, 1.91 cm Cyl)	88
25	Normalized Power Spectra of the P_w Fluctuation Amplitudes (FP, 1.91 cm Cyl)	89
26	Normalized Power Spectra of the P_w Fluctuation Amplitudes ($\gamma \approx .50$)	90
27	Dimensional Power Spectra of the P_w Fluctuation Amplitudes ($\gamma \approx .50$)	91
28	Normalized Power Spectra of the P_w Fluctuation Amplitudes ($\gamma \approx .50$)	92
29	Plot of Zero Crossing Frequency versus Intermittency (TF only)	93
30	Plot of Zero Crossing Frequency versus Intermittency	94
31	Probability Distribution of the Shock Periods	95
32	Probability Distribution of the Shock Frequency	96
33	Variation of Zero Crossing Frequency with Threshold Settings (1.91 cm Cyl, $\gamma \approx .50$)	97
34	Variation of Zero Crossing Frequency with Threshold Settings (1.91 cm Cyl, $\gamma \approx .70$)	98
35	Variation of Zero Crossing Frequency with Threshold Settings (1.27 cm Cyl, $\gamma \approx .50$)	99
36	Variation of Zero Crossing Frequency with Threshold Settings (1.27 cm Cyl, $\gamma \approx .70$)	100

LIST OF TABLES

Table	Description	Page
1.	Kulite Transducer Specifications	63
2.	Freestream and Boundary Layer Conditions	64

NOMENCLATURE

M_∞	freestream Mach number
δ_o	incoming boundary layer thickness
Re_∞	Reynolds number per meter
Re_θ	Reynolds number based on momentum thickness
U_∞	freestream velocity
δ^*	displacement thickness
θ	momentum thickness
Π	wake strength parameter
C_f	skin friction coefficient
U^+	non-dimensional velocity
Y^+	normalized wall coordinate
X	streamwise displacement
γ	intermittency
FS	Full Scale
a/d	analog to digital
D	diameter
S	separation line
T_o	stagnation temperature
P_o	stagnation pressure
\bar{P}_{bl}	mean boundary layer pressure
\bar{P}_w	mean wall pressure
P_{wt}	theoretical boundary layer pressure
σ_{Pw}	rms of the pressure fluctuations (standard deviation)
σ_{bl}	rms of the boundary layer pressure fluctuations (standard deviation)

α_{3bl}	skewness coefficient of the boundary layer pressure fluctuations
α_3	skewness coefficient of wall pressure fluctuations
α_{4bl}	flatness coefficient of the boundary layer pressure fluctuations
α_4	flatness coefficient of wall pressure fluctuations
f_c	zero crossing frequency
\bar{f}_i	mean shock frequency
T_i	shock period
T_m	mean shock period
T_r	delay time of shock passage between transducers
$(R_{pp})_{max}$	maximum cross correlation
τ	time delay at $(R_{pp})_{max}$
TF	tunnel floor
FP	flat plate
q_∞	freestream dynamic pressure
$\bar{\tau}_w$	mean wall shear stress
ζ	streamwise transducer spacing
d^+	normalized transducer diameter

CHAPTER 1

INTRODUCTION

1.1 Background

Since the onset of supersonic flight, shock wave/turbulent boundary layer interactions and boundary layer separation have become of primary interest and importance to vehicle designers and fluid dynamicists. Generation of shocks on high speed vehicles can occur for many reasons and at various locations including: in supersonic inlets; at external body junctions; at protuberances; and at control surfaces. These shocks may interact with other shocks generating shear layers or with the turbulent boundary layer causing separation and reattachment complications that cannot be neglected in the vehicle design. Large pressure fluctuations, caused by the unsteady motion of the separation shock wave can also create serious complications for vehicle control and performance, as well as the possibility of structural damage due to fatigue. Unsteady separation shocks in engine inlets lead to losses of stagnation pressure and cause unsteady flows at the compressor face; both have a detrimental effect on engine

performance.

A considerable volume of research over the past 30 years has been devoted to understanding the shock/turbulent boundary layer interaction process. It has been known for some time that shock induced turbulent boundary layer separation occurs with large scale, unsteady motion of the separation shock. Much of the early work[1-3]* in this area was concerned with the separation of the incoming boundary layer by shocks generated by steps and ramps. These studies were largely experimental and used photographic imaging, high speed cinematography, surface tracer techniques, and mean surface pressure measurements to characterize the separation process. However, results from such optical techniques are often difficult to interpret because they represent an integration of light across a flowfield with a randomly varying spanwise shock wave structure.[4] These techniques show the inherent unsteadiness of the shock structure but have provided mainly qualitative rather than quantitative information.

It is well established in incompressible turbulent flow that separation occurs over a region bounded by points of "incipient detachment" and "detachment", and not simply at one streamwise station.[4] In supersonic and hypersonic flows the process has not been documented and relatively little is understood about the dynamics of boundary layer

* Numbers in brackets refer to references.

separation. For example, in the shock/boundary layer interaction generated by blunt fins[5-6] and cylinders the separated flow is three-dimensional and highly vortical with vortex cores spiraling downstream rapidly. This complex structure, coupled with the unsteady shock motion and associated pressure fluctuations, makes it extremely difficult to study in real time. Because of this, much of the early work[5-9] in high speed flows consisted of mean flow measurements which provide little information about the interaction dynamics.

1.2 Recent Studies

With the advances in instrumentation and data acquisition systems, recent studies[10-26] have shed more light on the separation dynamics and a review of some of these efforts will be given in Chapter 2. The quantitative data consists mainly of wall pressure fluctuation measurements taken using several model configurations over a range of freestream flow conditions. These measurements are relatively easy to make but there are difficulties in interpretation of the signals. Questions have arisen due to the problems of spatial integration and resolution, which are a direct result of finite transducer size, as well as occasionally misleading results

from various conditional sampling techniques.

Despite these difficulties, recent studies employing both standard and innovative new analysis techniques, have helped document the shock-induced turbulent boundary layer separation process more fully. The major unresolved question is that of the driving mechanism behind the shock motion. The turbulence of the incoming boundary layer, the "pulsating" or "breathing" separation bubble behind the shock, or some combination of these as well as other factors have all been suggested as possible causes of the shock motion. Definitive proof for any of these is still lacking.

Studies using blunt fins[18-22], and cylinders[23-26] have given some indication that the shock motion is largely dependent on the diameter of the model (which, in turn, controls the scale of the separated region). Shock frequencies obtained from conditional sampling algorithms were much lower than the typical large eddy frequency of the boundary layer. Moreover, the shock frequency changed for different cylinder diameters in the same boundary layer. Overall, the influence of the incoming turbulent boundary layer on the shock motion appears to be small. However, other results[13-15] have indicated that the frequency depends on the incoming turbulent boundary layer. This apparent contradiction further clouds the issue of the driving mechanism.

1.3 Objective of Current Study

The purpose of the current study was to investigate the effect of the incoming turbulent boundary layer on the statistics of the shock motion in interactions generated by cylinders. It was hoped that this might contribute to an improved understanding of the driving mechanism. Tests were conducted in the University of Texas Mach 5 blowdown tunnel. In earlier work, Narlo[24] conducted tests on a flat plate using 1.91 cm (0.75 in) and 1.27 cm (0.5 in) diameter cylinders. This study will be discussed in more detail in Chapter 2. The current tests were made using the same cylinders mounted on the tunnel floor in the same facility, with an incoming turbulent boundary layer three times as thick. The freestream conditions were the same for both test series. Wall pressure fluctuation measurements were taken in both sets of tests and were analyzed using a conditional sampling algorithm developed by Narlo, and standard time-series analysis techniques. The role of Mach number was also investigated through direct comparison with Mach 3 data[20] using blunt fins.

An overview of recent related studies, and a detailed discussion of the experimental set-up and procedure are presented in Chapter 2 and Chapter 3 respectively. The discussion of results is included in Chapter 4 and the conclusions are presented in Chapter 5.

CHAPTER 2

LITERATURE REVIEW

2.1 Background

Over the past three decades numerous studies have investigated the shock wave/turbulent boundary layer interaction process. If strong enough, the interaction can cause separation of the boundary layer to occur. It is now well established that this is a highly unsteady phenomenon and the shock moves randomly at a relatively low frequency (compared to a typical eddy in the incoming turbulent boundary layer) and over a relatively large streamwise distance. Although a considerable amount has been learned about this process, many questions remain unanswered. Two questions of primary interest are: what are the dynamics of the unsteady shock motion; and what is the driving mechanism (or mechanisms) behind this motion?

2.1.1 Early Research

Efforts aimed at understanding shock-induced separation began in the early 1950's. Two of the earliest of these studies were by Bogdonoff and Kepler[1], and later Chapman *et al.* [2], who used micro-second spark schlieren photography, and high speed cinema to visualize the

wave structure of forward facing step-induced separated flows. As mentioned previously, these optical techniques are often difficult to interpret. However, these early results did provide some useful information which was, for the most part, qualitative. It was established without a doubt that the separation shock structure was unsteady.

Kistler[3], in 1964, was probably the first to measure the pressure fluctuations in a shock wave/turbulent boundary layer interaction, in this case generated by a forward facing step. Testing was conducted at nominal Mach numbers of 3.0 and 4.5. A piezoelectric pressure transducer was used to measure the pressure fluctuations caused by the shock motion and the output was observed on an oscilloscope. He concluded that the pressure signal could be described as large pressure fluctuations indicative of pressures downstream of the shock, superimposed on the smaller fluctuations characteristic of the incoming turbulent boundary layer.

Since the pressure fluctuation signal was observed and not recorded, Kistler was only able to describe the shock motion qualitatively as having a frequency smaller than 1 kHz. This value is at least one order of magnitude less than the large eddy frequencies ($f \approx U_e/\delta_o$) characteristic of the incoming turbulent boundary layer. Kistler felt that the most striking feature of the pressure signal was its characteristic step function appearance

which he reasoned was indicative of a moving shock. Figure 1 shows his representation of this pressure signal at different locations upstream of the step.

2.1.2 General Flow Characteristics

The pressure fluctuations observed by Kistler with a forward facing step have since been seen in studies using compression ramps[10-17], blunt fins[5-7,18-22], and cylinders[23-26]. The flowfields generated by these different models share some common characteristics. Each geometry generates a shock which can cause separation of the boundary layer and when this occurs a separation region or "bubble" results. In the case of cylinders and blunt fins,[5,6] the subsequent separated flow is composed of horseshoe shaped vortex cores near the surface which spiral downstream. The shock pattern that is formed in front of these protuberances has a characteristic lambda shape[5] (i.e., it is a normal shock away from the wall but bifurcates into two oblique shocks near the boundary layer). In contrast the separated region formed by unswept steps and compression ramps[10-17] contains a nominally two-dimensional recirculation zone with a large volume of lowspeed flow moving in the opposite direction to the incoming flow. Recent studies[12-15] have indicated that the instantaneous shock front in

these flows is non-uniform spanwise, giving it a rippling appearance.

A rise in centerline mean wall pressure (\bar{P}_w) occurs upstream of the model regardless of the model geometry; moreover, there is a similar increase in the rms of the pressure fluctuations (σ_{P_w}).^[4] Figure 2 and 3 show the typical distributions of \bar{P}_w and σ_{P_w} in the streamwise direction for compression ramps and blunt fins respectively. These figures show that the moving shock causes a rapid increase in σ_{P_w} . The maximum is a large fraction of \bar{P}_w , and occurs upstream of S (where S is the separation location indicated by surface tracer techniques).^[26] Since the separation shock is unsteady, the increase of \bar{P}_w in the streamwise direction occurs because stations further downstream are behind the shock at elevated pressures for a greater fraction of time.^[28] The traditional view that \bar{P}_w increases through a continuous compression fan is clearly incorrect.^[4] These general flow characteristics seem to be common to all shock induced separated flows regardless of Mach number and Reynolds number.

2.2 Shock Motion/Dynamics

Most of the data taken during the last 10-15 years have been in the form of mean flow measurements. These data provide evidence about mean flow characteristics (like \bar{P}_w); however, no quantitative dynamic information can be learned from this type of data. Within the last decade,

more advanced, high-speed data acquisition systems have become available and it is now possible to quantify the shock dynamics. In many recent studies[3,10-17,20-22,24] miniature high frequency response pressure transducers have been used to measure the wall pressure fluctuations generated by the passage of the shock. Test configurations have included steps, ramps, sharp-fins, blunt-fins, and cylinders to generate separation. These studies have provided some information concerning the dynamics of the interaction but have not identified the driving mechanism behind the shock motion. Most results indicate that the shock frequency is low (of order 1 - 2 kHz) which, as previously mentioned, is at least one order of magnitude lower than the large eddy frequencies typical of the turbulent boundary layer. Frequency as it is referred to here, is the "zero crossing frequency" (f_c) and indicates the number of shock crossings per second. These results confirm Kistler's earlier findings.

2.3 Recent Research

The remainder of this chapter will review several of the above studies which provide the most up to date information about the dynamics and driving mechanism of the shock motion.

2.3.1 Blunt Fin Results

Dolling, *et al.* [18,19] and Dolling and Bogdonoff[20,21] conducted experiments at the Gas Dynamics Laboratory at Princeton University. The tests were carried out in the high Reynolds number blowdown tunnel which has a cross-section of 20 cm x 20 cm and a nominal freestream Mach number of 3.0. Two blunt fins of diameter 1.27 cm (0.5 in) and 2.54 cm (1.0 in), were used. Mean surface pressure[18,19,21], and pressure fluctuation[20] measurements were taken using pressure tappings and high frequency response pressure transducers, respectively. Boundary layer thicknesses (δ_0) of 0.3 cm and 1.6 cm were obtained by conducting experiments on a flat plate and on the wind tunnel floor, providing a variation in δ_0 of about 5 to 1.

Based on their results, the authors concluded that:

1. The separation shock wave structure was highly unsteady and experienced random streamwise excursions over a distance of about one diameter.
2. The pressure fluctuation levels throughout the interaction region depended primarily on the fin leading edge diameter. They noted that, "at a given station, the larger fin diameter [generated] higher

intensity fluctuations.[20] Variations in boundary layer thicknesses have only a second order effect.

3. One of the three rms pressure fluctuation peaks on the centerline occurred upstream of separation and was caused by the shock motion. Peak rms levels at this point were 35-40 times the rms levels of the incoming turbulent boundary layer. Using the upstream rms level as a normalizer is misleading. The actual difference in rms values is probably lower because the pressure transducers almost certainly underestimated the rms value of the boundary layer by as much as 50% (see Section 3.4.1). This implies that the actual amplification in rms level is probably only a factor of 17. However, this is still a significant value.

The primary focus of these studies was not on the investigation of the driving mechanism behind the shock motion. However, the results do shed some light on the possible driving mechanism. Since the pressure fluctuation levels changed for different fin diameters and since the fin diameter determines the scale and structure of the separated region, it is likely that some feature of the separation region is involved in driving the shock motion.

2.3.2 Compression Ramp Studies

In a later study, Dolling and Murphy[10] measured wall pressure fluctuations under the oscillating separation shock in a 24 degree compression ramp interaction. These experiments were also conducted in the Princeton University wind tunnel, mentioned earlier. Boundary layer thicknesses of 1.25 cm and 2.21 cm were achieved by moving the ramp to different streamwise stations on the wind tunnel floor.

The intermittency (defined as the fraction of time that a given station is downstream of the shock) was calculated using a one-threshold conditional sampling algorithm. The threshold was set as $P_{bl} + 3\sigma_{bl}$ where (P_{bl}) is the mean boundary layer pressure and (σ_{bl}) is the standard deviation of the boundary layer pressure fluctuations. These values were determined in a separate test in which the boundary layer pressure fluctuations were measured without a model present. The zero crossing frequencies of the shock were found to be between 1 - 2 kHz, depending on the station used in the wind tunnel. The maximum zero crossing frequency decreased with increasing boundary layer thickness. This suggests some influence by the boundary layer on the shock motion. However, the authors also found that the frequencies of the shock motion decreased as the length of the separated flow region increased. This is similar to the result found in the blunt fin interaction above

and suggests a dependence on the scale of the separated region and/or its structure.

The results of this study[10] were similar to those found in the previous blunt fin studies. No suggestion was made concerning the probable driving mechanism behind the shock motion. There is some evidence that f_c is influenced by changes in δ_o and the scale of the separated region. However, once again it is worth noting that the frequencies of the shock were at least one order of magnitude less than the estimated large eddy frequencies of the incoming boundary layer. Obviously there is no clear correlation between the frequencies of the incoming boundary layer and the frequency of the shock motion. This result suggests a greater dependence on some mechanism other than the boundary layer.

This investigation was extended further by Dolling and Or[11] using ramp angles of 8° , 12° , 16° , and 20° . These tests were also conducted in the Princeton University wind tunnel with the ramps mounted on the tunnel floor, providing a δ_o of 2.2 cm. Fluctuating wall pressure measurements were taken using a single high frequency response pressure transducer. The results at all ramp angles were similar to those previously seen in the blunt fin studies and the earlier compression ramp study. The frequency of the shock was, in all cases, relatively low (1-2 kHz), and thus supports the same conclusion that

the shock motion is not dependent on the incoming boundary layer. Moreover, they found that the rms of the pressure fluctuations decreased with decreasing ramp angle, which is similar to the result[20] found by changing the fin leading edge diameter. The common link between these results is the scale of the separated region, which changes with either fin diameter or ramp angle and apparently affects the pressure fluctuations. This fact suggests the scale of the separated region also affects the shock motion.

In a similar study, Andreopoulos and Muck[13] also conducted tests at the Princeton University wind tunnel using 16° , 20° , and 24° ramps. The boundary layer was 2.4 cm thick. Four miniature in-line pressure transducers were used to measure the pressure fluctuations that were caused by the shock wave motion. The ramp was mounted on the tunnel floor and its position was moved relative to the transducers to vary their location within the intermittent region.

A one-threshold conditional sampling algorithm was used to analyze the pressure signals. By "eyeballing" a threshold level, the pressure fluctuations caused by the shock motion were separated from those typical of the boundary layer. This "eyeballing" was believed to eliminate any problems that could occur due to a DC offset in the pressure signal, which the authors believed was a problem with the tests conducted by Dolling and Murphy[10].

The threshold used in the latter study was set for all tests at one value based on the boundary layer statistics. Andreopoulos and Muck believed that these results would be biased if any DC shift occurred in the pressure signal without adjusting the threshold. Consequently, they chose a different threshold level for each test by first viewing the raw pressure signal and determining an "eyeballed" value.

From their results the authors concluded that:

1. The zero crossing frequency of the shock was of the same order as the bursting frequency of the incoming turbulent boundary layer.
2. The frequency of the shock motion was independent of the location in the intermittent region and independent of the ramp angle used (i.e., independent of the scale of the separated region).

These results prompted Andreopoulos and Muck[13] to suggest that "the incoming boundary layer was the most likely cause triggering the shock wave oscillation."

At this point it is useful to comment on the choice of conditional sampling algorithms. A complete discussion of these algorithms and their output is available elsewhere[26], but a brief outline is provided

below. Close examination of one and two-threshold algorithms (such as those used in the studies cited) suggests that one-threshold algorithms will always generate unrealistically high shock frequencies regardless of how carefully the threshold is chosen.[24-26]

The various conditional sampling algorithms convert the pressure signal into a square wave or "box car" form as shown in Figure 4, where T_i is the time between consecutive shock passages over the transducer, and is determined from this converted signal. Dolling and Brusniak[26] have shown that single threshold method algorithms always count "false shocks". Figure 4a show a typical pressure-time history. An example of an ideal box car conversion of this pressure signal is shown in Figure 4b (as judged by eye). A second example showing the conversion by a one-threshold method is presented in Figure 4c. It is evident that the one-threshold method converted several small fluctuations into box cars. These fluctuations are actually high frequency turbulent fluctuations associated with the boundary layer and their inclusion biases the mean and most probable frequencies to significantly higher values.

To avoid this problem Narlo[24] developed a two-threshold conditional sampling algorithm. As the name implies, this method uses two thresholds which are obtained from statistical analysis of the actual pressure

signal as follows:

1. The signal is analyzed to determine the mean pressure, P_{bl} , of that fraction of the signal corresponding to the undisturbed boundary layer.
2. Once P_{bl} is determined, σ_{bl} of the pressure fluctuations in the boundary layer is calculated.
3. The first threshold (T_1) is then set at $P_{bl} + 4.5 \sigma_{bl}$, and the second threshold (T_2) is set at P_{bl} .

T_1 was set at $4.5\sigma_{bl}$ above the mean because the probability of finding pressure fluctuations greater than this value is 0.0000068 or 1 chance in 147000.[20] When the pressure exceeds T_1 the shock is considered upstream of the transducer and the box car counter is started. This condition remains constant until the pressure falls below T_2 , indicative of the shock moving downstream of the transducer, and the box car counter is reset to zero. Figure 4d shows a two-threshold signal conversion of the pressure signal seen in Figure 4a. It is observed that the "false shock" counting is largely eliminated. The sensitivity of f_c to the threshold settings was examined and the results are included in the Appendix.

With the above in mind, it is evident that only two-threshold conditional sampling algorithms should be used. The conclusions drawn by

Andreopoulos and Muck[13] are questionable at best, due to the bias present in a one-threshold conditional sampling algorithm. Their results are a direct contradiction of the findings of Dolling and Murphy[10], further clouding the issue of the shock driving mechanism.

Tran[18] conducted a test program in the same facility as above using two model geometries: a 20° unswept compression ramp and a sharp fin at angles of attack of 10° , 12° , 16° , and 20° . The boundary layer thickness was 1.7 cm. High frequency response pressure transducers were used to measure the wall pressure fluctuations. Tran used a two point correlation technique in the compression ramp tests. This method used two transducers; one upstream to sense events present in the boundary layer and a second downstream to sense events in the intermittent region. Using this set-up, he attempted to correlate those events on the upstream transducer with those detected by the downstream transducer.

Tran concluded that there was little correlation between the events in the turbulent boundary layer and the low frequency events associated with the intermittent region. He also used the VITA (variable interval time averaging) conditional sampling technique to analyze the pressure fluctuations in the intermittent region. This analysis confirmed the previous findings of the two-point correlation technique (i.e., no evidence was found that suggested the

incoming boundary layer was driving the shock oscillation). The results of the fin tests (at angles of attack) also confirmed these results. He concluded that the shock unsteadiness was triggered by some mechanism other than the turbulent boundary layer.

Further tests were conducted by Muck, Andreopoulos, and Dussauge[15] using compression ramps with angles of 16° , 20° , and 24° , in the Princeton University wind tunnel. The boundary layer thickness was 2.4 cm. Wall pressure fluctuations caused by the shock oscillation were measured using an array of four miniature pressure transducers.

They concluded that:

1. Upstream of the mean separation line, the flow was dominated by a single shock wave undergoing large scale motion of the order of δ_0 .
2. The shock front was non-uniform in the spanwise direction, and was significantly three-dimensional.
3. The incoming turbulent eddies, which were convected into the interaction, were the cause of this three-dimensional shock front.
4. In the separated region, the energy containing turbulent eddies above the separation bubble were the

major cause of the wall pressure fluctuations.

These data confirm their earlier findings[13] and once again suggest that the incoming turbulent boundary layer is the main cause of the shock motion. However, the authors did notice that the frequency of the shock motion changed with different shock strengths (i.e., ramp angles) which is contrary to their previous findings. Part of the original argument[13] that the incoming turbulent boundary layer was the primary cause of the shock motion, was the fact that the shock frequency was the same for all ramp angles. The authors interpreted that to indicate that the separation region had no effect on the shock motion. The new results showed this was not the case, and thus the original conclusions[13] were thus even more questionable.

2.3.3 Cylinder Results

Narlo[24] measured the wall pressure fluctuations under an unsteady separation shock wave/turbulent boundary layer interaction in a Mach 5.0 flow. These tests were conducted at the University of Texas blowdown wind tunnel facility. Circular cylinders of diameter 1.27 cm (0.5 in) and 1.90 cm (0.75 in) were mounted on a full-span flat plate which was at zero angle of attack. Two miniature, 0.159 cm diameter, Kulite pressure transducers mounted flush with the plate surface were used to measure the wall pressure fluctuations. The cylinder was moved relative to the pressure

transducers to improve spatial resolution. The author noted that the change of incoming flow conditions had negligible effect on the interaction scale and properties.

Narlo's tests were conducted as a direct result of the findings of Andreopoulos and Muck. These tests were designed to shed some light on the still unanswered question of the shock driving mechanism. Narlo attempted to do this by first determining the range of frequencies of the shock motion, and then correlating these results with the various flowfield parameters. A two-threshold conditional sampling algorithm was used to analyze the pressure data.

Based on the results the author concluded:

1. The zero crossing frequency, f_c , was a function of position in the intermittent region and reached a maximum at an intermittency of about 0.5.
2. f_c was a function of the cylinder diameter (D); f_c increased as D decreased.
3. f_c was a maximum of 1.2 kHz for the 1.90 cm cylinder and 1.6 kHz for the 1.27 cm cylinder. These values were two orders of magnitude less than the typical large eddy frequency and one order of

magnitude less than the estimated turbulent bursting frequency.

These results led Narlo to infer that the shock wave motion was not driven by the incoming turbulent boundary layer. Instead, Narlo concluded that the shock motion was a function of the cylinder diameter, or stated differently, a function of the scale of the separated region. These conclusions were, for the most part, contrary to those found by Andreopoulos and Muck[13]. However, they supported the results reported by Dolling and Bogdonoff[20] as well as Dolling and Murphy[10]. Several studies mentioned above indicated that the pressure fluctuations were weakly affected by changes in the incoming boundary layer (to second order). With this in mind, Narlo's statement that the shock motion was not a function of the incoming boundary layer seems inappropriate, especially since his tests were conducted in only one boundary layer.

2.3.4 Additional Studies/Analyses

Narlo and Dolling[25], carried out additional analysis that compared the Mach 5.0 cylinder results with the Mach 3.0 blunt fin results obtained by Dolling and Bogdonoff[20]. This provided a direct comparison of similar model geometries in different Mach number flows, as well as different boundary layer thicknesses. The same two-threshold conditional sampling

algorithm was applied to the Mach 3.0 data. The two model geometries produced the same general trends.

The authors concluded that:

1. f_c was dependent on the cylinder or blunt fin leading edge diameter and decreased as D increased.
2. For a fixed D , f_c was independent of the incoming boundary layer thickness over a variation in thickness of 5 to 1.
3. The average upstream and downstream shock wave velocities were calculated to be about 20% of the broad-band convection velocity in the incoming turbulent boundary layer.

This comparison prompted Narlo and Dolling to conclude again that the low frequency of the shock wave motion coupled with the low shock wave velocities did not support the conclusion that the motion is triggered by turbulence in the incoming boundary layer. They reasoned that the shock motion is in some way coupled with the lower frequency pressure fluctuations in the downstream separated flow. However, the conclusion that f_c was independent of the incoming boundary layer is probably incorrect. This conclusion was based on insufficient results which lacked spatial resolution.

Recent analysis[26] of this and other data has shown that there is some effect on the zero crossing frequency due to changes in the incoming turbulent boundary layer. Also, the third conclusion above was drawn from cross-correlations. It has since been shown[26] that the calculated velocities are not actually average values, but maxima.

In a similar study, Dolling and Brusniak[26] examined and re-evaluated some of the published data on unsteady shock-induced turbulent boundary layer separation. Wall pressure fluctuation measurements taken under the oscillating separation shock produced by compression ramps, blunt fins, sharp fins, and cylinders were evaluated. The results of this analysis supported those reported earlier by Narlo and Dolling[25] except these authors noted the influence of the boundary layer on f_c . They suggested a link between the low velocity fluid at the upstream edge of the separated region and the shock motion. This conclusion was based on results[28,29] found in computational studies. The predicted flow structure reported in these studies showed a subsonic region existed at the upstream edge of the separated region which becomes larger and has lower velocities as the boundary layer becomes thicker. Dolling and Brusniak suggested that this might help explain why f_c changed not only for different cylinder diameters at a constant δ_0 , but also for a constant D and changing δ_0 . They reasoned that the latter occurred because

of the different details in the structure of the separated region of the two boundary layers.

Based on these results, Dolling and Brusniak also stated that no evidence existed which linked the low shock frequency to the characteristic frequencies of the incoming turbulent boundary layer. However, these results do imply that the incoming turbulent boundary layer indirectly influences the shock motion by changing the structure of the separated region.

2.4 Summary

In summary, it must be said that, despite the considerable number of experiments carried out to date, the mechanism responsible for the shock unsteadiness is still not known. It seems most likely that the scale and "pulsing" of the separated region is connected with the shock oscillation. The data also suggest that the incoming turbulent boundary layer has only second order effects. Despite numerous tests, the data base is still inadequate and most conclusions concerning the driving mechanism are largely speculation.

It is for these reasons that the current effort was undertaken. Pressure fluctuations under the oscillating separation shock in interactions induced by circular cylinders were measured using high frequency response pressure transducers. The flow conditions were identical to those used by Narlo[24], but tests were conducted on the tunnel floor. This provided a δ_o

which was three times as thick as that used by Narlo. By duplicating all test conditions except δ_o , it should be possible to determine the effects the boundary layer has on the shock motion.

CHAPTER 3

EXPERIMENTAL PROGRAM

3.1 Test Facility

Testing was conducted in the University of Texas at Austin, Balcones Research Center, Mach 5 Blowdown Tunnel. The tunnel has a cross-section of 17.8 cm x 15.2 cm (7 in x 6 in) and a nominal free stream Mach number of 5.0. The air storage tanks, which can be pressurized up to 2550 psig, are capable of storing about 140 ft³ of air. This air is then heated by 18 banks of nichrome wire heaters upstream of the tunnel stagnation chamber. Stagnation pressure is monitored and controlled using a Moore MYCRO 352 Single-loop Digital Controller that allows the pressure to be maintained within 1% of the set-point. Stagnation temperature is controlled with a Love Controls Corporation model 1543 controller that maintains the temperature within 2 °F.

3.2 Incoming Flow Conditions

More than 150 tests were carried out at a Mach number of $4.90 \pm .02$ at the test station. All tests were conducted at a nominal stagnation pressure of 304 psia $\pm 1\%$ and a stagnation temperature of $595^{\circ}\text{R} \pm 1^{\circ}\text{R}$

corresponding to a free stream unit Reynolds number of about $55 \times 10^6 \text{ m}^{-1}$ ($16 \times 10^6 \text{ ft}^{-1}$). All tests were carried out under approximately adiabatic wall temperature conditions. Careful attention was given to maintaining the freestream conditions as near as possible to those used in Reference 24 so that differences between the two test series would be minimized and any change in results could then be attributed to the differences in the two boundary layers. The undisturbed boundary layer was "surveyed" using a flattened tip pitot probe with a tip height of 0.0305 cm (0.012 in).

3.3 Model

Figure 5 shows the model configuration. Two stainless steel, unswept cylinders, mounted on the test surface, were used to generate the interaction. Their diameters were 1.27 cm (0.5 in) and 1.91 cm (0.75 in) and their heights were 7 diameters and 4 diameters respectively. During an earlier test program in the same facility Westkaemper[8] determined that for a height to diameter ratio greater than 1.13, the separation location is independent of the cylinder height and the cylinder can be considered as semi-infinite. This criterion was generalized by Sedney and Kitchens[9] and again by Dolling and Bogdonoff[31] who specified that a height to diameter ratio of about 2.4 was needed to assume a semi-infinite condition. Each of the model heights satisfied this condition. The cylinders could be moved

streamwise to change the relative distance between the cylinder and the pressure transducers, which were at a fixed position in the test surface (see Section 3.4.1). This arrangement provided good spatial resolution and allowed accurate characterization of the intermittent region. The overall change in location of the cylinder from its original location was about 2 cm. Hence, the incoming boundary layer properties were essentially constant for all tests since a 2 cm change in streamwise position corresponds to a change of about 0.3 mm in the boundary layer thickness. Further, the mean properties in these types of flows are extremely insensitive to the incoming boundary layer conditions.

3.4 Pressure Transducers

3.4.1 Specifications

Wall pressure fluctuations were measured using two Kulite model XCW-062-15A (0-15 psia) pressure transducers. Table 1 lists the transducer specifications. These were the same transducers used in the earlier program of Narlo[24] and about three-fourths of the current tests were conducted with them. Both transducers were mounted 0.292 cm (0.115 in) apart in a 2.54 cm (1.0 in) diameter brass plug that was installed flush with the tunnel floor. Because of physical limitations, this was the closest the transducers could be placed together. The plug was placed in the test section,

upstream from and along the center line of the cylinder.

Each transducer was 0.163 cm (0.064 in) in diameter and had a pressure sensitive diaphragm of 0.071 cm (0.028 in) in diameter that had a fully active Wheatstone bridge atomically bonded to it. Shewe[32] performed fluctuating wall pressure measurements in zero pressure gradient subsonic flows and showed that σ_{P_w} will be underestimated if the diaphragm is too large. He found that σ_{P_w} normalized by the freestream dynamic pressure (q_∞) was a function of the normalized transducer diameter (d^+), where $d^+ \equiv du_r/v$. Shewe determined that the "ideal" transducer should have a value of $d^+ \leq 20$. The transducers used for this experiment were the smallest commercially available and had a d^+ of about 160. Dolling[25] estimated that by extrapolating Shewe's results, the measured σ_{P_w}/q_∞ should be about 40 - 50% of the "ideal" transducer. It is important to note that this criterion of 20 is for measurements in a zero pressure gradient turbulent boundary layer. For measurements in the shock interaction region, this restriction will not be as critical since previous studies have shown that the frequency of the shock motion is typically of order a few kHz. The transducer frequency response is further attenuated to about 50 kHz because of the protective outer

screen used to shield the diaphragm from dust particles.

In several studies[20,33] the effect of transducer flushness on \bar{P}_w , σ_{P_w} , and spectral content was investigated. The results showed that all these parameters were in error when the transducer was protruding into the flow. The studies also showed that a recessed transducer had significantly less error and, hence, was preferable to a protruding transducer. It was important, therefore, to insure that the cylinders were indeed flush with the test surface, or at worst, slightly recessed. This was accomplished by mounting the transducers under a microscope.

About one-fourth of the test program was conducted using two Kulite model XCQ-062-50A, (0-50 psia) pressure transducers mounted in the same manner as described before. Table 1 also lists the specifications for these transducers. Their usable frequency range was again estimated to be 50 kHz, because of the protective outer screen. The transducers provided a worst case overall signal resolution of 0.0016 psi/count (0 - 15 psi transducers) and 0.0006 psi/count (0 - 50 psi transducers).

3.4.2 Calibration of Transducers

The transducers were calibrated statically using the tunnel calibration rig. This rig permitted a wide range of pressure to be applied to the transducers. The pressures were measured using a Heise digital pressure

gauge that has an accuracy of .001 psi. This gauge was checked regularly to insure that no zero drift had occurred. Raman[34], in a study using a shock tube, showed that static calibrations were within a few percent of dynamic calibrations for transducers of this type. It was believed, therefore, that static calibration was sufficiently accurate for this program. Calibration of the transducers was conducted daily before the start of testing.

3.5 Additional Instrumentation

Figure 6 shows a block diagram of the instrumentation. The output signals from both transducers were amplified, using Measurements Group Inc. Model 2300 Amplifiers, with a gain of 100 - 2300 depending on the particular test and transducer model. These amplifiers had variable gain ranging from 1.0 to 10000, and provided transducer excitation voltage in the range 0 - 15 V. Since the amplifiers contained signal filters, they were operated in a wide-band mode. This allowed all frequencies up to 125 kHz to be passed to two Ithaco Model 4213 Electronic Filters. These were operated in a lowpass mode with a cutoff frequency of 50 kHz. This signal was then input to a Masscomp MC-500 series minicomputer having a 12 bit, analog to digital (a/d) converter which is capable of sampling one channel at a rate of 1 MHz. Multiple channels could be sampled using a sample-and-hold capability which samples all of the channels simultaneously and holds

the data long enough to record it, before taking another data point. Most runs were conducted using two channels sampled at 200 kHz per channel, obtaining 200 records of data per channel (1024 datapoints per record). All data were initially stored in memory, then transferred to computer disk and magnetic tape. A detailed explanation of the data acquisition software is provided in Reference 23.

3.6 Test Procedure

3.6.1 Separation Location

The first experimental step was to locate the separation line (S) and this was done using surface tracer techniques. The location of S is typically 2 - 2.5 D upstream of the cylinder, independent of Mach number.

Under no-flow conditions a lampblack-kerosene-diesel fuel solution was painted at many locations across the tunnel floor upstream of the cylinder. Under the action of the wall shear stress the mix moves downstream and into the interaction region. The mix has effectively zero frequency response and eventually dries on the tunnel floor leaving a surface streak pattern with a well-defined line, usually interpreted as the separation line, S. A typical flow example is shown in Figure 7. With careful examination of Figure 8, it is possible to see S as well as evidence of "backflow" behind the shock (i.e., flow moving upstream from the cylinder

toward S in the separation region).

Gramman and Dolling[35] described S as the downstream boundary of the region of intermittent separation. They developed a simple model on the assumption that the surface streaks responded to the mean wall shear stress ($\overline{\tau_w}$). They postulated that $\overline{\tau_w}$ could act in the downstream direction even when the flow was separated for a large fraction of the time.

3.6.2 Electronic Noise Estimation and Reduction

After the data acquisition instrumentation was installed it was necessary to identify and then eliminate or reduce noise within the system. In previous experiments at this facility, local radio frequency interference was noted on the signal lines. To alleviate this problem all equipment was grounded and cabling was routed through a channel in the concrete floor. Noise levels were then determined at the input to the a/d converter on each channel, using an oscilloscope. The noise detected was about 18 - 25 mV peak to peak (7 - 10 counts on the a/d converter). The resulting signal-to-noise ratio varied from 10:1 when measuring the boundary layer pressure fluctuations, to 100:1 when measuring those in the interaction region.

3.6.3 Boundary Layer Surveys

The next step involved boundary layer pitot surveys and transducer checks with no model in the tunnel. Tests were conducted at several sampling rates with transducers mounted spanwise and streamwise. Some results of this analysis are included in Table 2 where the standard deviation, skewness, and flatness are presented as σ_{bl} , α_{3bl} , and α_{4bl} respectively. Results for the boundary layer used in Reference 24 are also provided. Additional results from the boundary layer analysis are presented in Section 4.2.2.

3.6.4 Intermittent Region

After measuring the boundary layer properties, the pressure fluctuations in the intermittent region were measured. Intermittency was calculated throughout the interaction region using a two-threshold conditional sampling algorithm (see Section 2.3.2). Statistical analyses, sensitivity studies, power spectral measurements, conditional sampling analyses, and space-time correlations were then performed on the data.

CHAPTER 4

RESULTS AND DISCUSSION

4.1 Overview

This study was conducted in two parts, one beginning in October 1986 and the other in April 1987. This allowed the initial data to be analyzed, and also identified areas where additional data were still needed. The second set of tests then filled these data gaps. In both parts, the data consisted of wall pressure fluctuation measurements taken under the shock-induced separation generated by circular cylinders of diameter 1.91 cm (0.75 in) and 1.27 cm (0.5 in).

The objective of this study was to determine the effects of D and δ_o on the shock dynamics and to learn more about the driving mechanism of the shock motion. The flow conditions used in the current study were the same as those used in an earlier study[24], except for the different boundary layers. Through a direct comparison of results, the effects of the incoming turbulent boundary layer on the shock motion could be identified. The data were analyzed using standard time-series and conditional sampling techniques. The results are presented below.

4.2 Incoming Flow Analysis

4.2.1 Boundary Layer Analysis

The freestream and boundary layer properties for both test programs are presented in Table 2. Figures 8 and 9 show the mean velocity profiles in the form U/U_∞ versus Y/δ_0 and in wall coordinates, U^+ versus Y^+ , for all four cases. The static pressure and total temperature were assumed to be constant through the boundary layer. Although the surveys[30] were conducted immediately downstream of a region of strong favorable pressure gradient (i.e., the nozzle), the deduced skin friction value (C_f) agrees quite closely with the Van Driest II prediction using M_∞ and Re_θ as inputs. C_f was also deduced from the U^+ versus Y^+ fitting routine and from Preston tube measurements[37] (Tunnel floor only). All values of C_f determined from these methods were within $\pm 7\%$ of the mean value.[37] The wake strength parameter (Π), however, was approximately $1/3 - 1/2$ of the zero pressure gradient value and is due to the favorable pressure gradient upstream.[30] The fullness of the velocity profile (Figure 8) shows this effect. The FP boundary layer develops in a zero pressure gradient. Consequently, Π for the FP boundary layer is within the accepted range for equilibrium turbulent boundary layers. The broadband convection velocities, (U_c) can be calculated if ζ (the streamwise spacing between transducers) and

τ at $(R_{pp})_{\max}$ are known (where τ is the time delay at $(R_{pp})_{\max}$, and $(R_{pp})_{\max}$ is maximum in the cross correlation). U_c was $0.67U_\infty$ and $0.72U_\infty$ for the TF and FP boundary layers, respectively.

Power spectral density plots for both boundary layers are shown in Figure 10. The data are plotted in the form $f(G(f))$ versus f on linear-log axes. This figure shows that both boundary layers have little low frequency noise contamination. Closer examination shows that most of the power in the signal occurs at higher frequencies, as expected, and the tunnel floor (TF) case increases in power level at slightly lower frequencies than the flat plate (FP) results. This is also expected since the estimated large eddy frequency ($f \approx U_\infty/\delta_o$) in the tunnel floor turbulent boundary layer is less than that in the flat plate turbulent boundary layer (approximately 45 kHz and 135 kHz respectively). The cut-off just beyond the maxima that occurs in both spectra is due to the Ithaco filter, which had a cutoff frequency of 50 kHz. Much higher frequencies exist in the turbulent boundary layer. This can be seen in Figure 11 which shows the power spectra for data taken in the TF boundary layer with the filter cutoff frequency set at 100 kHz. As expected energy level continues to rise beyond the cutoff frequency in Figure 10. It is important to note that the data in Figure 11 were taken with the 0 - 50 psi transducers which were theoretically able to accurately measure frequencies

up to about 100 kHz. However, this is true only if the outer protective screen is not attached. This screen, as previously mentioned, tends to attenuate the transducer frequency response. With this in mind, Figure 11 is questionable at the very high frequencies but is presented for qualitative purposes.

The probability distribution of the pressure fluctuation amplitudes in the incoming turbulent boundary layer, is presented in Figure 12. The pressure fluctuation amplitudes in the boundary layer are random and distributed normally. This is expected of a transducer whose $d^+ = 160$ (see Section 3.4.1).

In summary, taking into account the different histories of each turbulent boundary layer, there are no unusual features. This is true despite the spatial resolution and bandwidth limitations caused by the transducer size. Analysis of the test data can therefore be made with some confidence that no anomalies in the boundary layer are influencing the results.

4.2.2 Flow Visualization Results

As previously mentioned (Section 3.6.1), the separation location (S) was determined using a lampblack-kerosene-diesel fuel mix. The resulting pattern was lifted from the tunnel floor with a sheet of clear tape (Figure 7). S is usually very distinct in these patterns. The line is not formed by an accumulation of lampblack, but is a dividing line which

appears due to the difference in shading in the two regions it separates.[20] S was located at $X/D = -2.20$ for the 1.91 cm cylinder and at $X/D = -2.30$ for the 1.27 cm cylinder. These values compare well with results of several earlier studies[8,20,24], using cylinders and blunt fins, in which S was found in the range $X/D = -2.0$ to -2.65 .

These patterns can also be used to determine the extent of the upstream influence of the shock motion. The lampblack patterns show that the incoming streamlines are parallel. The line along which these streamlines first turn spanwise is the line of upstream influence. This is more difficult to locate on the lampblack patterns because it is not as clearly defined as S and this method is obviously subjective. For the current flows the upstream influence was determined to be at $X/D = -2.80$ and -2.90 for the 1.27 cm and 1.91 cm cylinders respectively. These values the same as those found in the earlier flat plate study.[24]

The line of upstream influence coincides with the streamwise location at which \bar{P}_w first increases. Using this method, upstream influence was found at $X/D = -2.85$ and -2.9 for the 1.27 cm and 1.91 cm cylinders respectively. These values agree very well with the surface flow visualization and also agree with those found in the flat plate study.

4.3 Intermittent Region Analysis

4.3.1 Flow Characteristics

Figures 13 and 14 show the distributions of \bar{P}_w and σ_{P_w} in the streamwise direction for both cylinders and for both the tunnel floor (TF) and flat plate (FP) results. The mean pressure data in Figure 13 are presented in normalized form (\bar{P}_w/P_{wt}), given by:

$$\left(\frac{\bar{P}_w}{P_{wt}}\right) = \frac{(\bar{P}_w - P_{bl}) + P_{wt}}{P_{wt}}$$

where (\bar{P}_w/P_{wt}) is the normalized value, P_{bl} is the boundary layer pressure determined from the conditional sampling algorithm, and P_{wt} is the theoretical static pressure calculated at Mach 4.9 using isentropic relationships. This normalization was done to correct for drift in the transducer output. At these low static pressures and with small temperature shifts, drift is unavoidable. Note, however, this does not affect the sensitivity, so drift has no effect on the quantitative fluctuating pressures. The data for $D = 1.91$ cm and $\delta_o = 1.61$ cm, have been plotted on the correct (X/D) scale. For clarity, each successive line has been offset by $X/D = 0.5$ from its original value. The limit of upstream influence, described in Section 4.2.2, can be seen in this figure. All of the pressure data follow a similar

trend regardless of changes in δ_o or D .

Figure 14 shows that a similar rise in σ_{Pw} also occurs. These data have also been offset the same amount as in Figure 12. The maximum σ_{Pw} is about 0.33, regardless of changes in δ_o or D . Both the normalized pressure and σ_{Pw} exhibit the same qualitative trends as seen in compression ramp and blunt fin induced interactions (Figures 2 and 3).

Plots of σ_{Pw} versus γ (intermittency) are shown in Figure 15. For a given δ_o (i.e. tunnel floor or flat plate) and a fixed intermittency, σ_{Pw} increases as D increases, indicative of a stronger separation shock. Also, for a given D , σ_{Pw} decreases with increasing δ_o .

The flatness coefficient as a function of γ is shown in Figure 16 for both cylinders on the tunnel floor. The data are essentially identical in all cases. The skewness coefficient as a function of γ is shown in Figure 17 for both cylinders and for both boundary layers. The shaded band represents the range of data from Mach 3.0 blunt fin and 2-D compression ramp interactions. The agreement is good overall, bearing in mind that the values of γ in the Mach 3.0 studies were determined using a one-threshold conditional sampling algorithm which gives values of γ that are lower than those found with a two-threshold method. If the values of γ for the 2-D ramp and blunt fin interactions had been determined using a two-threshold method

algorithm, then the shaded band would shift to higher values. Thus, within engineering accuracy, there is no difference between the development of the skewness coefficients at Mach 3 and 5.

Figure 18 shows the distributions of γ as a function of X/D for all test cases. The trends are identical with γ first increasing near the line of upstream influence and reaching unity near the separation location. This is the same trend as in several earlier studies (blunt fin and 2-D compression ramp). The length scale of the intermittent region for all cases was about $0.8D$. This, too, is the same as the earlier studies.

All the results discussed above for both the TF and FP flow conditions are qualitatively and quantitatively very similar. This observation is important because it implies that the separation shock behavior is consistent for many flows, at different Mach numbers, and in different facilities. Also the close agreement with other interactions shows that the two flows have no unusual features that are a function of this facility.

4.3.2 Probability Distributions of Pressure Fluctuation Amplitudes

Sample wall pressure signals for the 1.97 cm cylinder at values of $\gamma \approx .30$ and $\gamma \approx .70$ are shown in Figures 19a and 20a. Large amplitude, low frequency pressure fluctuations are consistent with measurements in earlier studies. Even for such a short time span, it can be

seen that as γ increases the time between shocks decreases, as expected. The probability distributions of the pressure fluctuation amplitudes at the values of γ quoted above, are shown in Figures 19b and 20b. The distribution at $\gamma = .30$ is highly skewed with a well defined maximum. At this low value of γ , a greater percentage of time (approximately 70%) is spent within the pressure range of the turbulent boundary layer. The shock-induced pressure fluctuations raise the mean to a value which is slightly higher than \bar{P}_w . Hence, as seen in Figure 20b the greatest probability is about 0.5 standard deviations below \bar{P}_w .

The probability distribution at $\gamma \approx .70$ shows a similar but slightly different result. Now, there are two noticeable maxima in the distribution, one above and one below \bar{P}_w . It is important to note that at this value of γ , a greater percentage of time (approximately 70%) is spent at elevated pressures downstream of the shock. Since these elevated pressures are also randomly distributed, and have large amplitude in terms of σ_{P_w} of the entire signal, the probability peak is much broader and less defined, but never-the-less identifiable. Since these elevated pressures are greater than \bar{P}_w , the probability peak indicative of the shock pressures is centered about

1.0 standard deviation above the mean.

The second peak in this figure is more pronounced and occurs about one standard deviation below the mean. This peak is caused by the pressure fluctuations in the turbulent boundary layer. Even though the signal is at these pressures for only 30% of the time, the probability of finding a pressure within the range of the turbulent boundary layer is still much greater.

These trends in the raw pressure time-histories and the probability distributions of the pressure fluctuation amplitudes (Figures 19 and 20 above) are consistent throughout the intermittent region, for both test cases. The same results were seen in the flat plate study[24], as well as several previous studies.

4.3.3 Power Spectral Density Plots

4.3.3.1 Evolution of the Power Spectra at Different Intermittencies

Power spectra for the 1.91 cm cylinder, at various values of γ are shown in Figures 21 and 22. The data in these figures are presented using two different formats. Figure 21 is plotted on linear-log axes in the form $f(G(f))$ versus f , where $G(f)$ is the power level and f is the frequency. When plotted in this form, the spectral coefficients are weighted by their respective frequencies. This method makes it easier to identify the relative

contribution of each frequency band to the total variance, "highlighting" any dominant frequencies.

This figure shows that a common narrow-band dominant frequency exists for the power spectra at the various values of γ ($\gamma = .10, .30, .50, .70$, and Separated Flow). It is evident that as γ increases, the power in the signal also increases, but the dominant frequency range in each spectra falls within a narrow band of about 600 - 900 Hz. This frequency range represents broadly the frequency of the larger amplitude shock-induced pressure fluctuations throughout the intermittent region. It is important to note that the center frequency (or peak frequency) is not the zero crossing frequency, defined in Section 2.2. Instead, the center frequency is the frequency of the largest amplitude pressure fluctuations at that specific γ .

Figure 21, above, is consistent with the results seen in Figures 18 and 19, mentioned earlier. The rise in power that occurs at the center frequency as γ increases is implied by the time-histories. This is because as γ increases both the percentage of time spent at elevated pressures behind the shock and the number of shock crossings, increase. Also the percentage of larger amplitude pressure fluctuations increases. Thus the power at the center

frequency increases.

Figure 22 is plotted in the form $f(G(f))/\sigma_{P_w}^2$ versus f . The advantage of using this format is that by normalizing $f(G(f))$ with $\sigma_{P_w}^2$, the area under each curve is forced to unity. The data in this figure show that the spectra are essentially the same, with a dominant frequency range of 600 - 900 Hz. Figure 23 shows the same normalized data seen in Figure 22 but in this case the lower curve has been plotted on the axes shown and each successive curve has been shifted upward by increments in $f(G(f))/\sigma_{P_w}^2$ of 0.15. This format allows the shift in the center frequency to be seen. As γ increases, the center frequency tends to decrease. This is logical since as γ increases the shock fluctuations become much larger and there is more power at these lower, large amplitude frequencies.

Figure 24 and 25 show spectra for the 1.91 cm cylinder, through the intermittent region in the FP flow, and are plotted in the same way as Figures 21 and 22. The trends are the same but the center frequency range is slightly higher, between 900 - 1600 Hz. These higher frequencies, in the thinner boundary layer flow, indicate that some change does occur due to changes in boundary layer properties. However, this increase in frequency range is not large compared to the change in typical eddy frequency (about

3:1), suggesting only second order effects from the boundary layer.

Also shown in Figures 21 and 22 are the power spectra of the pressure signal in the separated region (0.292 cm downstream of S). These spectra are quite different from those in the intermittent region. However, there is a peak in the same frequency range as that of the shock so there is definitely low frequency, large amplitude pressure fluctuations within the separated region. Since the center frequency of the low frequency band is the same as those of the intermittent region, it is quite probable that they are related. However, without additional analysis it is difficult to determine whether the peak in the separated case occurs because of the shock motion (i.e. the separation bubble flapping behind the shock) or whether it is the cause of the shock motion. Both are possible but neither is discernible from the present data.

Also evident in the separated flow power spectra is the presence of higher frequencies as well. This broad range of frequencies is generated by eddies in the separated turbulent shear layer. As shown in Figure 21, the the larger fraction of the overall variance is generated by the high frequency eddies. At these frequencies (ranging from 20 - 50 kHz), the spectra looks very similar to that of the turbulent boundary layer seen in Figure 10.

4.3.3.2 Power Spectral Density Plots at $\gamma \approx .50$

Figures 26 and 27 show the normalized and dimensional power spectra at $\gamma \approx .50$ for the four test cases (this includes the two test cases shown earlier in Figures 22 and 24). The different diameter cases plotted in Figures 26 and 27 have different center frequencies. The normalized data of Figure 27 show this trend more clearly. It is seen that, for a constant δ_0 , the center frequency of the 1.27 cm cylinder is higher than that of the 1.91 cm cylinder. This is true for both data sets (1.0 kHz and 0.7 kHz respectively, for the TF data: 1.6 kHz and 1.0 kHz respectively, for the FP data). At a constant D , a decrease in δ_0 causes an increase in the center frequency.

Figure 28 shows the same normalized data on expanded axes. Again, the bottom line has been plotted on the correct axes and each successive line has been offset by $f(G(f))/\sigma_{P_w}^2 = 0.15$. The dependence of the center frequency on both δ_0 and D is again clearly evident, although it is not large.

4.3.4 Zero Crossing Frequencies

Figure 29 shows the zero crossing frequency (f_c) versus γ for both cylinder diameters in the floor boundary layer. As D decreases there is an increase in f_c . In both cases the maximum value of f_c occurs at about $\gamma \approx$

.50 and are approximately 950 Hz and 1200 Hz for the 1.91 cm and 1.27 cm cylinders respectively.

Figure 30 shows f_c versus γ for all test cases. The same trend (increasing f_c with decreasing D) can be seen for the FP data, as well. However, for a fixed D , f_c also increases as δ_o decreases.

The trends seen in Figures 29 and 30 are the same trends seen in the power spectra in Figures 26 and 27. f_c changes when both D and δ_o change. However, the change in f_c is not large. The maximum values of f_c occur at low frequencies (1 - 1.6 kHz).

These results were determined using a two-threshold conditional sampling algorithm. It is encouraging to see that using a completely different method of analysis the same results as seen previously with the power spectra, are obtained.

4.3.5 Probability Distributions of the Shock Periods

Figure 31 shows the probability density distributions of the shock wave periods (T_i) at $\gamma \approx .50$, for all four cases. The vertical axis is given by:

$$\left(\frac{N_i}{N_t}\right) \left(\frac{1}{W}\right) = \text{Probability (kHz)}$$

where N_i is the number of shocks within a given range, N_t is the total number of shock periods, and W is the width of each interval in seconds. The

interval size is chosen to reduce the scatter in the data without significantly affecting the resolution and was done by incorporating several intervals of datapoints into one. Fluctuations in a given interval are averaged providing a mean value of N_i/N_t , (which is then multiplied by $1/W$), and a mean period.

The lowest curve in Figure 31 is plotted on the axes shown and each successive curve is offset by $(N_i/N_t)(1/W) = 0.8$, for clarity. The floor data have been plotted with an interval of $20 \mu\text{s}$ while the plate data are plotted with an interval of $10 \mu\text{s}$.

The choice of interval size must be made cautiously so that the data are not biased by averaging the points in several intervals into one. The difference in interval width for the floor and plate flows, above, is a result of the number of data records in each case. For the floor tests 200 records were taken while in the plate tests 400 records were taken. The larger sample size allows the statistics of the pressure fluctuations to be more accurately resolved. Consequently, the floor data required a larger interval for better resolution.

The mean period (T_m), which is the inverse of the zero crossing frequency) is indicated by the arrows on each line. T_m follows the same trends with D and δ_o that were seen before with the power spectra center frequencies at $\gamma \approx .50$ (Figures 26 - 28). All of the distributions have

the same shape and the same general trends. For a fixed δ_o , the maximum shock period decreases as D decreases (4 ms and 3 ms for the TF 1.91 cm and 1.27 cm cylinders respectively, and 3 ms and 2 ms for the FP 1.91 cm and 1.27 cm cylinders respectively). Also, for a fixed D , the maximum shock period decreases as δ_o decreases (4 ms and 3 ms for the 1.91 cm cylinders in the TF and FP flows respectively; 3 ms and 2 ms for the 1.27 cm cylinders in the TF and FP flows respectively).

The most probable period (T_p), for the data shown in Figure 30, is basically the same for all four cases. Given the scatter in the data for each case, $T_p \approx 0.5$ ms.

4.3.6 Probability Distributions of the Shock Frequencies

Figure 32 shows the probability density distributions of the shock frequencies (f_i), at $\gamma \approx .50$, for all four cases. It is important to note that since $f_i \equiv 1/T_i$, the distributions of f_i and T_i are not linearly related, thus the mean frequency \bar{f}_i is given by:

$$\bar{f}_i = \frac{1}{N} \sum_{i=1}^N \frac{1}{T_i} \neq \frac{1}{T_m}$$

The distributions are plotted in the same format as Figure 31 above. However, W (the interval width) for these plots is no longer a constant but is given by:

$$W = \left(\frac{1}{T_i} - \frac{1}{T_i + \text{interval}} \right)$$

The chosen interval size is again a compromise between resolution and scatter.

The cases in Figure 32 exhibit the same general shape and trends. The most probable frequency, for each case, falls within a narrow frequency range (approximately 0.7 kHz to 1.5 kHz). This is the same frequency range of the center frequencies of the power spectra (Figures 26 - 28). The mean frequency is shown by an arrow on each curve and in each case is close to the most probable frequency. Figure 32 shows that for a fixed D , both the mean and most probable frequencies decrease with increasing δ_o . For a fixed δ_o , the mean and most probable frequencies decrease with increasing D . These are the same trends seen in the analysis of the power spectra.

4.3.7 Calculation of Shock Speeds

Shock velocities in both the upstream and downstream directions were calculated, for all four test cases, by Baade and Dolling[36]. By knowing the delay time (T_p) of the shock passage between the two transducers, as well as the transducer spacing, the shock speeds can be determined. Baade and Dolling found that the mean upstream and downstream shock speeds are very low ($0.06U_\infty$ - $0.07U_\infty$). These speeds are considerably lower than the broadband convection velocities (U_c) of the

incoming turbulent boundary layers.

4.4 Implications of Results

The changes that occur due to changing D and changing δ_o are not large. It is evident that these factors do influence the shock motion, D more so than δ_o , but both seem to have only second order effects. The low shock frequencies and long periods seen in the above analysis, suggest that the shock motion is not tied directly to the higher frequency fluctuations of the turbulent boundary layer. For a fixed D , a change in δ_o by a factor of three, with a consequent change in large eddy frequency of a factor of three, does not change the frequency of the shock motion by a factor of three. Also, since the shock frequencies are at least one order of magnitude less than the large eddy frequency of the incoming turbulent boundary layer, and in the plate case two orders of magnitude, it is not likely that the shock is convected by these incoming eddies. It is also likely that the velocity fluctuations are not generated by them either. Moreover, the very low upstream and downstream shock speeds for both test cases are much lower than U_c and further indicate that the shock motion is not driven by the incoming turbulent boundary layer.

A more likely cause of the shock motion is the pressure fluctuations within the separated region. Power spectra of the separated

region showed that large amplitude pressure fluctuations behind the shock were in the same frequency range as that of the shock motion. It is not possible, based on the current data, to say conclusively whether these low frequency pressure fluctuations, seen in the separated flow spectra, are the cause of the shock motion or are caused by the shock motion. However, since the equilibrium position of the separation shock within a given flow is determined by the pressures on either side of the shock, it seems likely that the pressure fluctuations within the separated region could cause the shock to oscillate about the equilibrium position. Since the pressure fluctuations are *continuous and random*, the shock oscillation is also continuous and random. This issue has been explored by Dolling and Baade[36] using a 1-D analysis of a moving shock wave, and the predicted shock speeds are in close agreement with the measured values. The quantitative results of the present study, notably the shock frequency distributions, provide further support for this idea.

CHAPTER 5

CONCLUSIONS

An experimental study has been made of unsteady shock-induced turbulent boundary layer separation caused by unswept circular cylinders, at Mach 5. Wall pressure fluctuations were measured using two high frequency response, miniature pressure transducers. The data were analyzed using standard time-series analysis and conditional sampling analysis techniques. Comparisons were made with results from an earlier test program in which cylinders were mounted on a flat plate and tested under identical freestream conditions, but with a thinner boundary layer (factor of 3 in thickness). The results of the analysis shows:

- 1) The shock zero crossing frequency (f_c) was a function of the cylinder diameter, as observed in the earlier flat plate studies, suggestive of some connection with the downstream separated flow rather than the incoming turbulent boundary layers. The maximum values were 1.2 kHz for the 1.27 cm cylinder, and 0.95 kHz for the 1.91 cm cylinder. f_c is a function of position in the intermittent region and is a maximum at an intermittency of 0.50.

- 2) The zero crossing frequency is also dependent on the the incoming turbulent boundary layer. The change in the incoming boundary layer thickness was about 3:1 which causes a change in the large eddy frequency by the same factor. However, the change in the zero crossing frequency was only about 20%.
- 3) Shock frequencies for all test cases (both tunnel floor and flat plate) were within a narrow frequency band from 0.7 - 1.6 kHz. These frequencies are at least one order of magnitude (or more) less than the large eddy frequencies of the turbulent incoming boundary layer. The most probable shock period was about 0.5 ms for all cases and the most probable frequency was in the neighborhood of about 1 kHz.
- 4) The small change in shock dynamics which occurs due to a large change in incoming turbulent boundary layer properties, shows that the incoming boundary layer has only second order effects. It does not appear to be the primary shock driving mechanism. The same is true of changes in the scale of the separated region (caused by changes in cylinder diameter).
- 5) Low frequency pressure fluctuations within the separated region may well be the most likely cause of the shock motion. These low frequency pressure fluctuations are within the same frequency band as those of the shock. However, the current data were

insufficient to substantiate this idea. Additional focused testing in this area is recommended.

CHAPTER 6

APPENDIX

6.1 Threshold Sensitivity Study

Figures 33 and 34 show the results of the sensitivity study conducted on the threshold settings for the two-threshold conditional sampling algorithm. The data are at nominal values of $\gamma \approx .50$ and $.70$ respectively, for the 1.91 cm cylinder in the floor flow. The different curves are for different T_2 thresholds. The lower curve in each figure is for $T_2 = \bar{P}_{bl}$ and each successive curve above is for T_2 incremented by one standard deviation (i.e., curve 2 is for $T_2 = \bar{P}_{bl} + \sigma_{bl}$). At the same time T_1 is determined by incrementing \bar{P}_{bl} by 'n' multiples of σ_{bl} . In this way a record of the changes in f_c based on changes in T_1 and T_2 can be determined. The two-threshold algorithm used in the current study had T_1 and T_2 set at $\bar{P}_{bl} + 4.5\sigma_{bl}$ and \bar{P}_{bl} respectively (shown by an arrow on each plot).

Figure 33 shows that f_c does change based on the choice of T_1 and T_2 , however, the change is not large. For a given T_1 , f_c changes only slightly when T_2 is varied from $\bar{P}_{bl} + 4.5\sigma_{bl}$ to $\bar{P}_{bl} + 9.0\sigma_{bl}$. The same is

true for a constant T_2 and different T_1 values.

Figure 34, which is for $\gamma \approx .70$, exhibits the same trends mentioned above. Figures 35 and 36 show the results of the 1.27 cm cylinder, in the TF flow ($\gamma \approx .50$ and $.70$ respectively). The trends for these figures are identical to the previous trends seen above.

As γ increases, the changes in f_c tend to become more sensitive to the threshold settings. This is expected since, as γ increases, the time between shocks decreases and the two-threshold algorithm has a slightly greater chance of error. Such errors occur when, given two threshold settings, the pressure fluctuations exceed T_1 (indicating a shock moving upstream) but before the pressure drops back below T_2 (indicating the shock moving back downstream), another shock passage occurs. In this case the two-threshold algorithm counts two shock passages as one. Obviously, this problem is worse when more and more pressure fluctuations due to the shock occur within a given time frame (i.e., when γ increases). This effect is evident from Figures 33-36.

Overall, the data show that f_c does not change by a large amount (approximately 10% - 20%) over a wide range of different threshold settings. Although this implies that f_c cannot be determined exactly, the fact that the sensitivity of f_c to T_1 and T_2 is low, indicates that the f_c values are

reasonable, and of the right magnitude. Therefore, the consistent use of one set of threshold settings will allow the range of shock frequencies to be accurately modeled.

Kulite Pressure Transducer Specifications		
Parameter	XCW-062-15A	XCQ-062-50A
Rated Pressure (psi)	15	5
Over Pressure (psi)	45	15
FS Output (V)	225	75
Excitation (V DC)	15	5
Max Change in Sensitivity w/ Temperature	8%/100 °F	±2%/100 °F
Natural Frequency (kHz)	250	600
Max Change No-Load Output w/ Temperature	2% FS/100 °F	
Combined Nonlinearity and Hysteresis	0.5%	
Repeatability	0.1% FS	
Zero Balance	3% FS	
Compensated Temp Range	80 °F to 180 °F	
Operating Temp Range	-65 °F to 250 °F	
Resolution	Infinite	

Table 1 Pressure Transducer Specifications[Reference 24]

Wind Tunnel Flow Conditions		
Parameter	Tunnel Floor	Flat Plate
M_∞	$4.90 \pm .02$	$4.96 \pm .02$
U_∞	741 m/s (2432 ft/s)	739 m/s (2424 ft/s)
Re_∞	$53.3 \times 10^6 \text{ m}^{-1}$ ($16.2 \times 10^6 \text{ ft}^{-1}$)	$53.1 \times 10^6 \text{ m}^{-1}$ ($16.2 \times 10^6 \text{ ft}^{-1}$)
T_0	330°K (595°R)	327°K (590°R)
P_0	$2.09 \times 10^6 \text{ N/m}^2$ (304 psi)	$2.09 \times 10^6 \text{ N/m}^2$ (303 psi)
X	0.74 m (29 in) from throat	0.33 m (13 in) from leading edge
δ_0	$1.62 \times 10^{-2} \text{ m}$ (0.63 in)	$5.36 \times 10^{-3} \text{ m}$ (0.25 in)
δ^*	$5.23 \times 10^{-3} \text{ m}$ (0.206 in)	$2.18 \times 10^{-3} \text{ m}$ (0.086 in)
θ	$4.54 \times 10^{-4} \text{ m}$ ($1.83 \times 10^{-2} \text{ in}$)	$1.81 \times 10^{-4} \text{ m}$ ($7.13 \times 10^{-3} \text{ in}$)
π	0.115	0.47
Re_θ	23.4×10^3	8.99×10^3
C_f	9.9×10^{-4}	1.01×10^{-3}
P_{bl}	0.646	0.600
σ_{bl}	1.02×10^{-2}	8.0×10^{-3}
α_{3bl}	0.110	.007
α_{4bl}	3.363	--

Table 2 Freestream and Boundary Layer Conditions[Reference31,24]

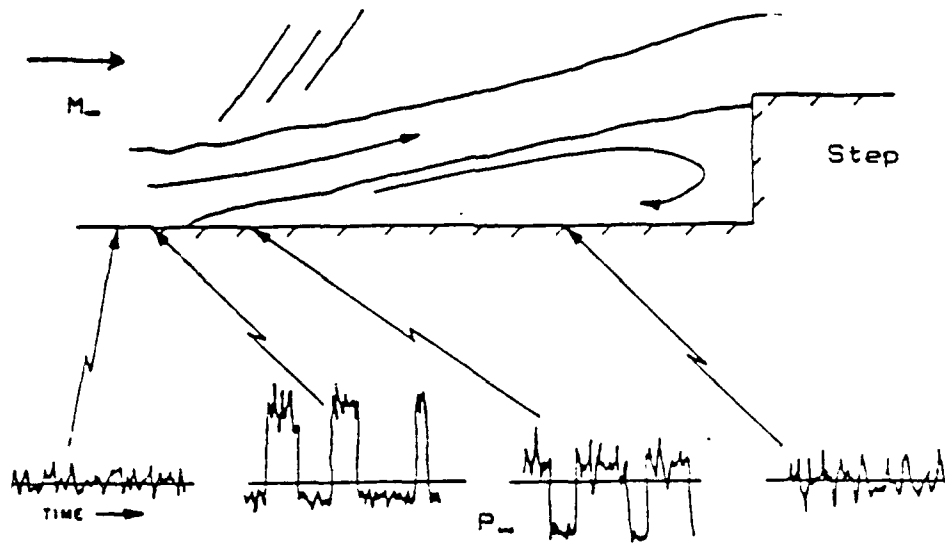


Figure 1 Pressure Fluctuations in Front of a Forward Facing Step
(Reference 3)

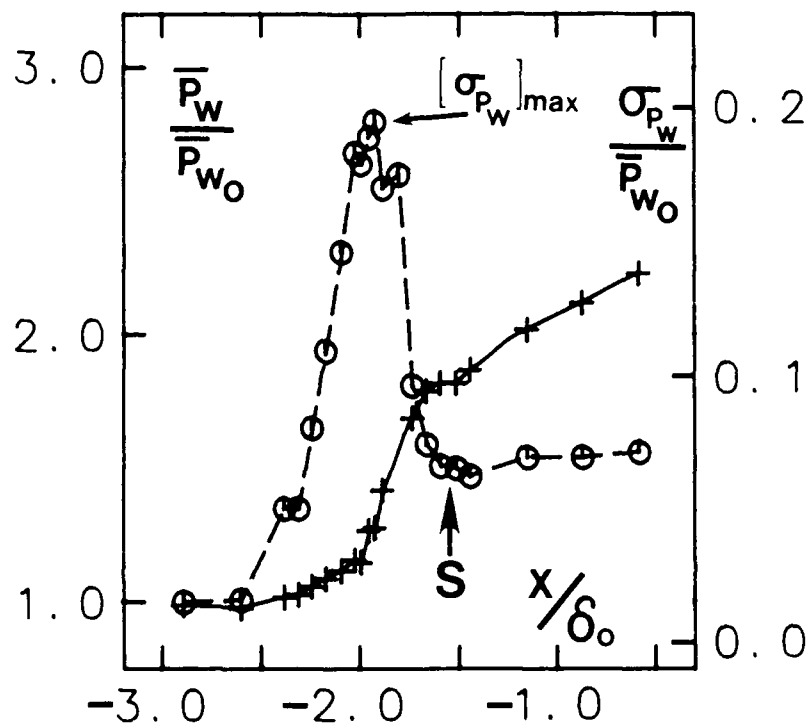


Figure 2 Distribution of P_w and σ_{P_w} in Compression Ramp Flowfield (Reference 26)

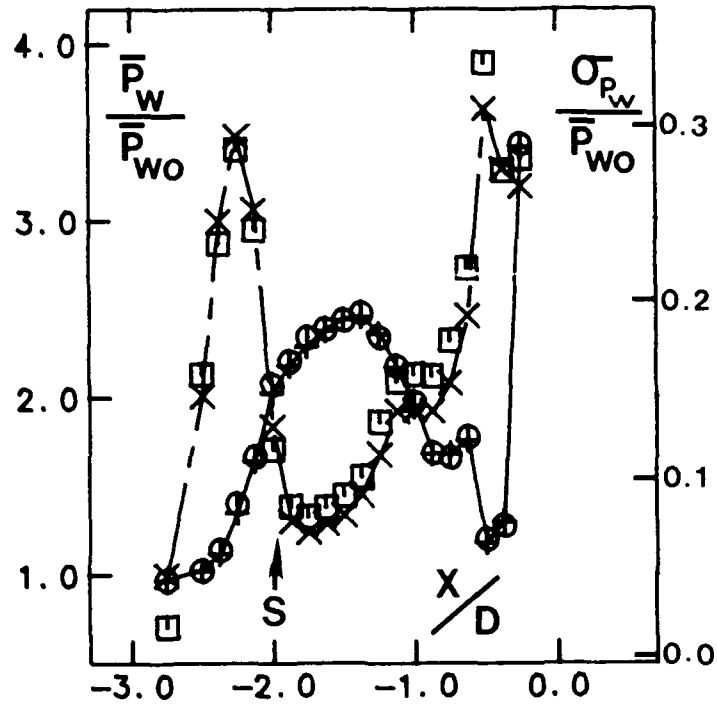


Figure 3 Distribution of P_w and σ_{P_w} in Blunt Fin Flowfield
(Reference 26)

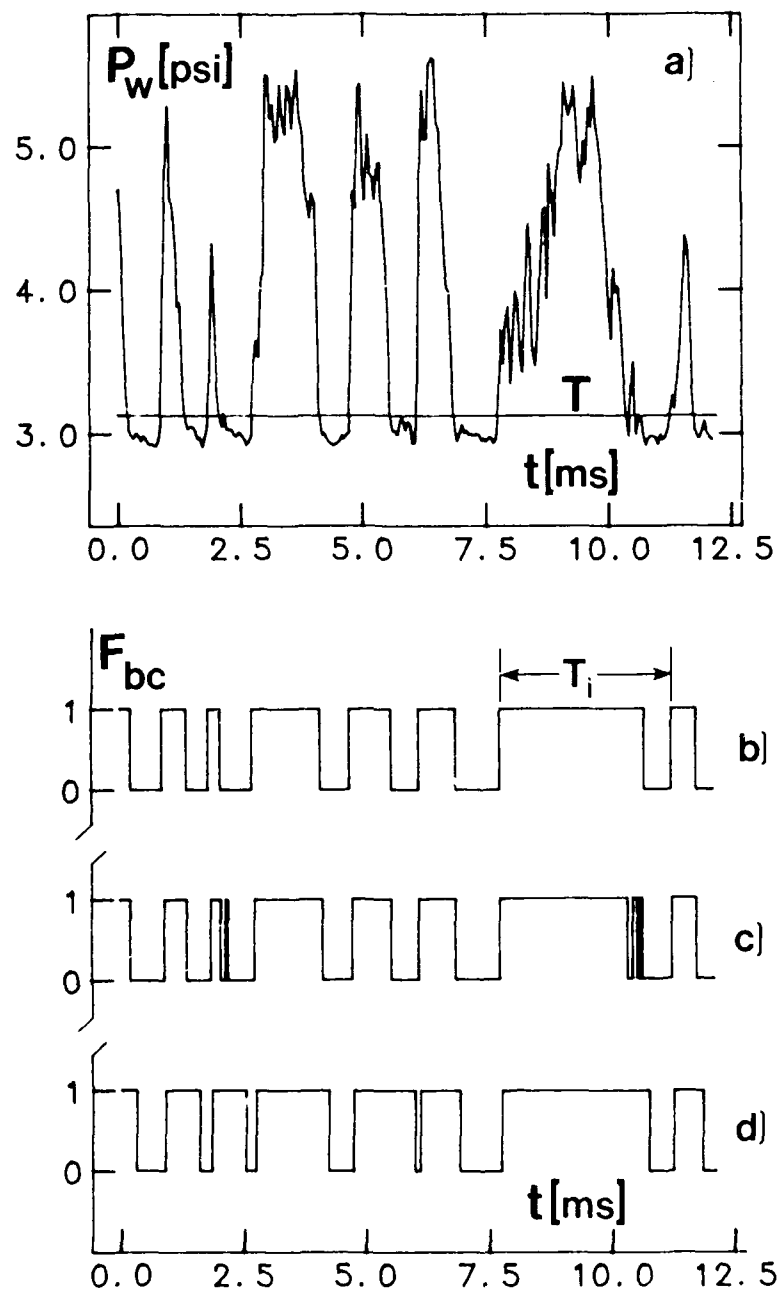
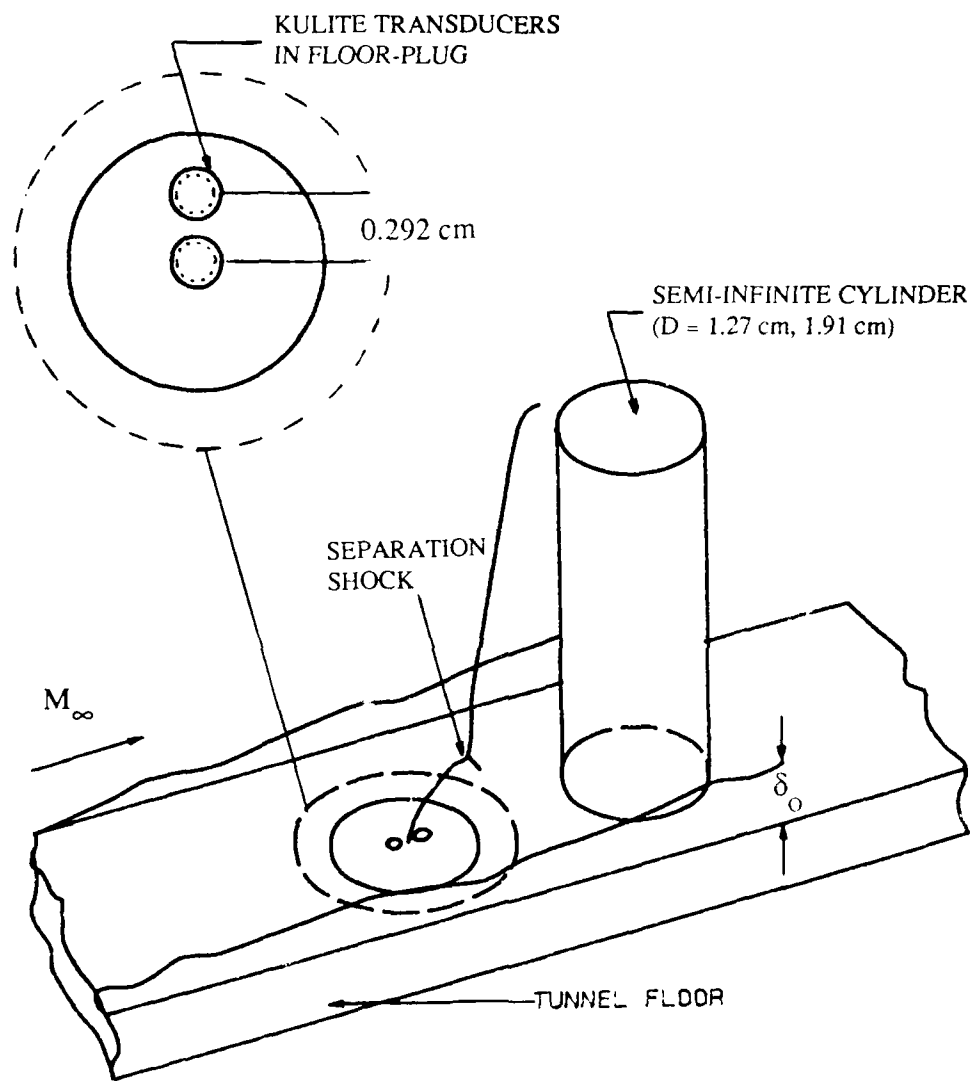


Figure 4 Conversion of Pressure Signal into Box-Car Function
(Reference 26)



NOTE: DRAWING NOT TO SCALE

Figure 5 Test Configuration

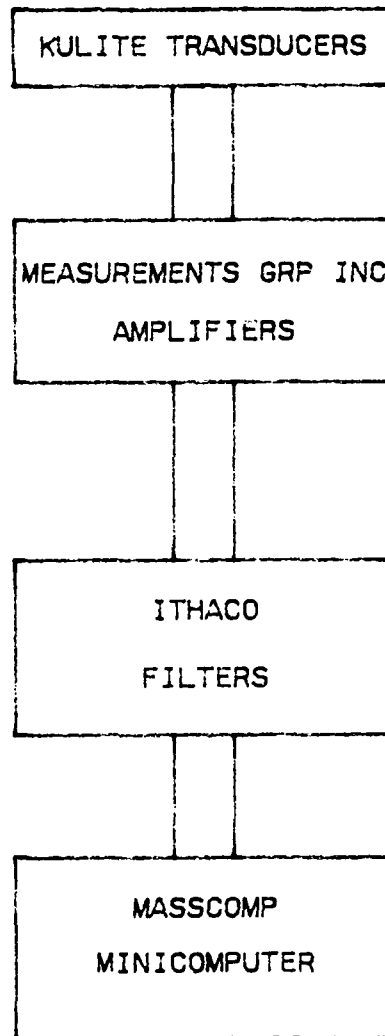


Figure 6 Instrumentation Block Diagram

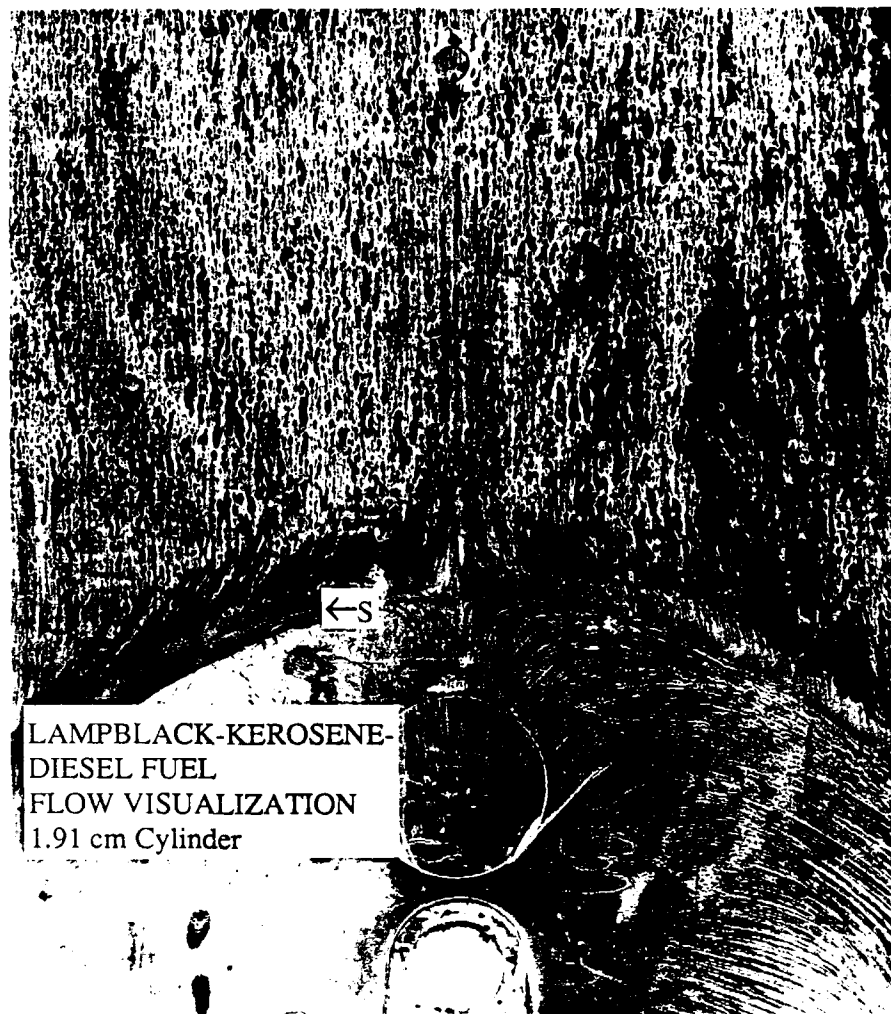


Figure 7 Typical Flow Visualization Pattern

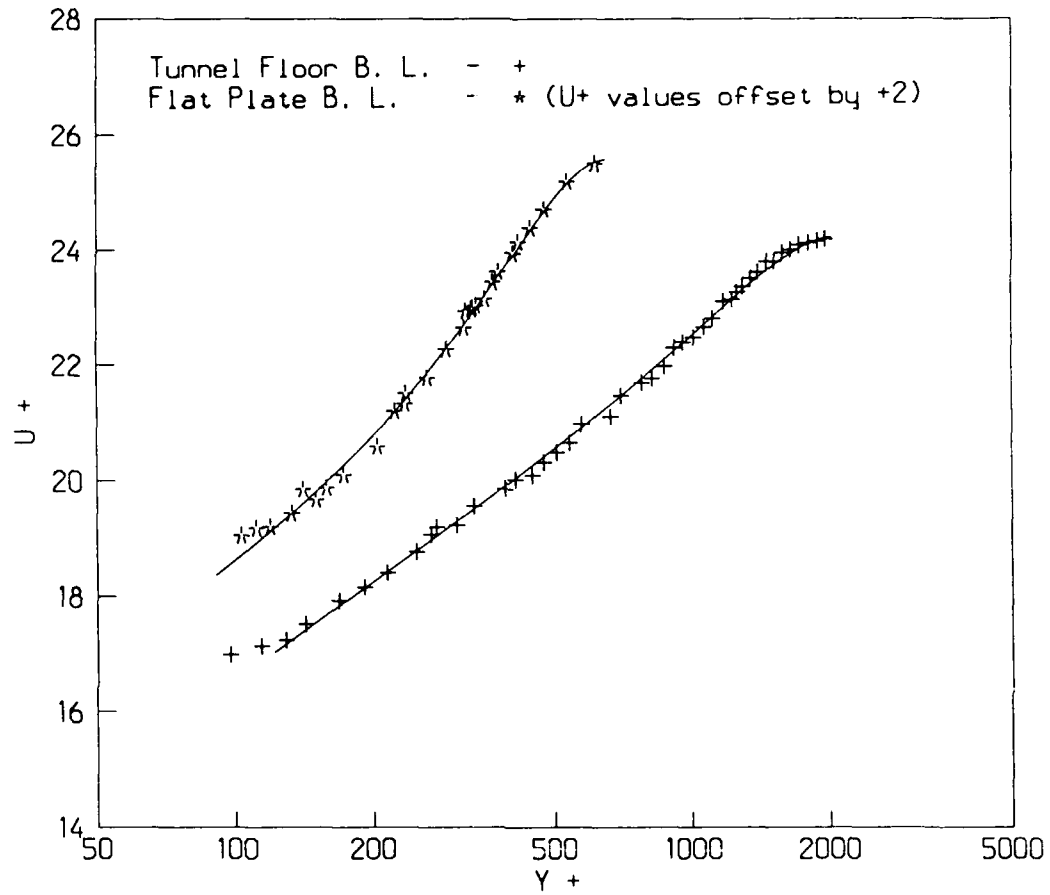


Figure 8 Mean Velocity Profiles in Wall Coordinates (Reference 36)

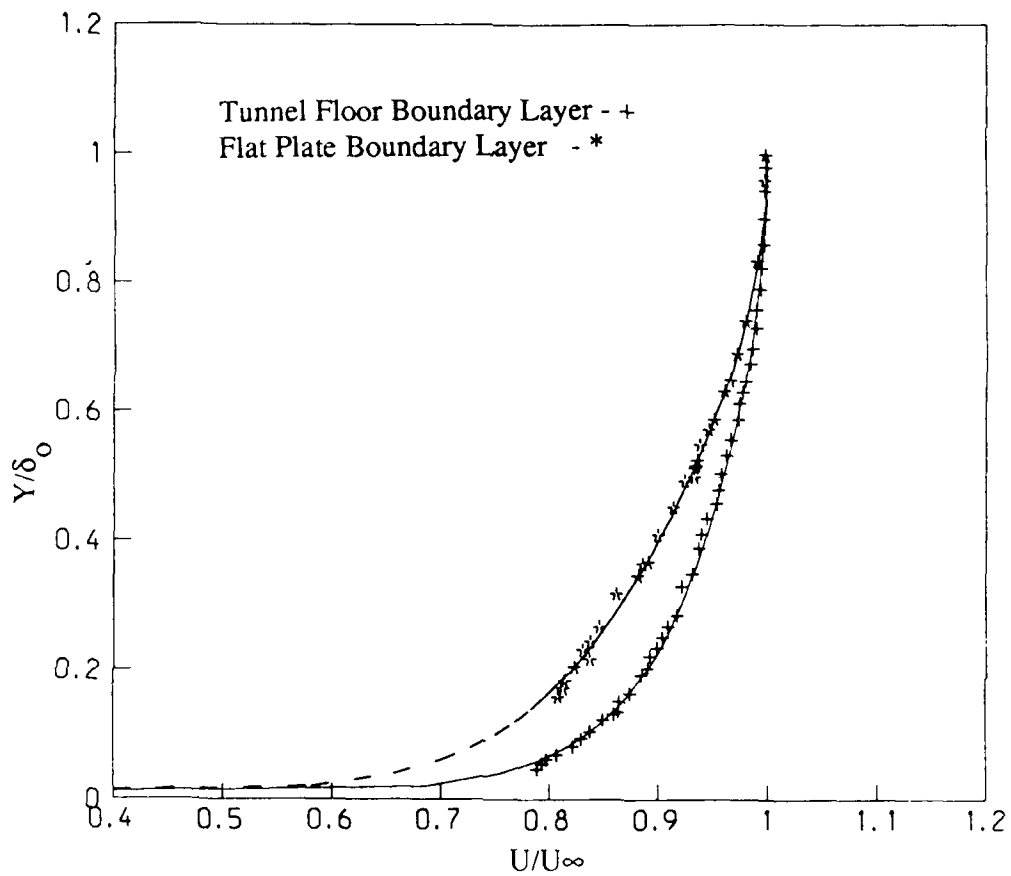


Figure 9 Mean Velocity Profiles (Y/δ_0 vs U/U_∞ , Reference 36)

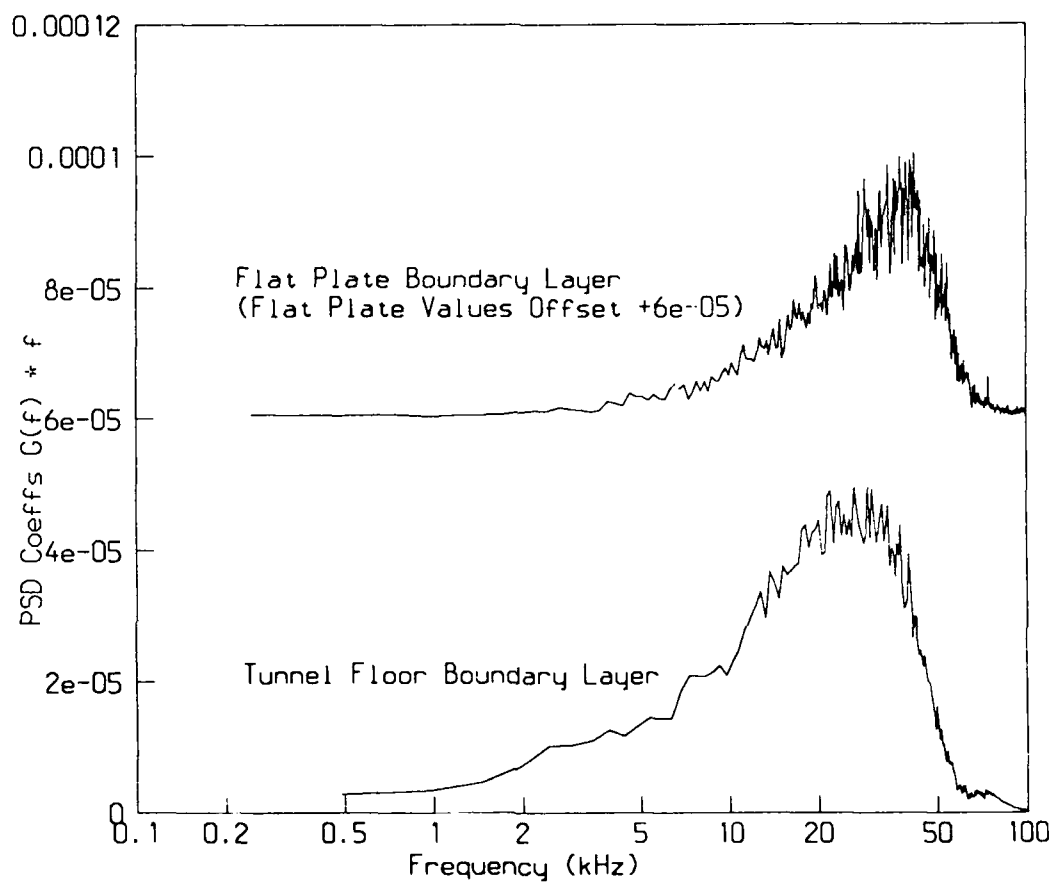


Figure 10 Power Spectra of the Boundary Layer P_w Fluctuation Amplitudes

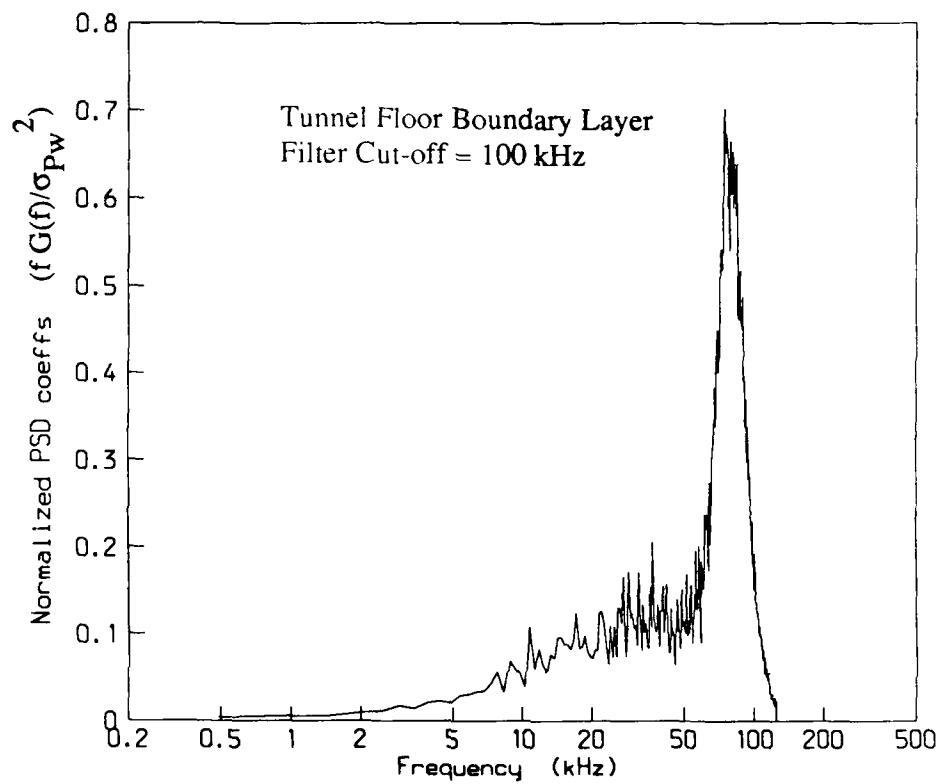


Figure 11 Power Spectra of the Boundary Layer P_w Fluctuation Amplitudes

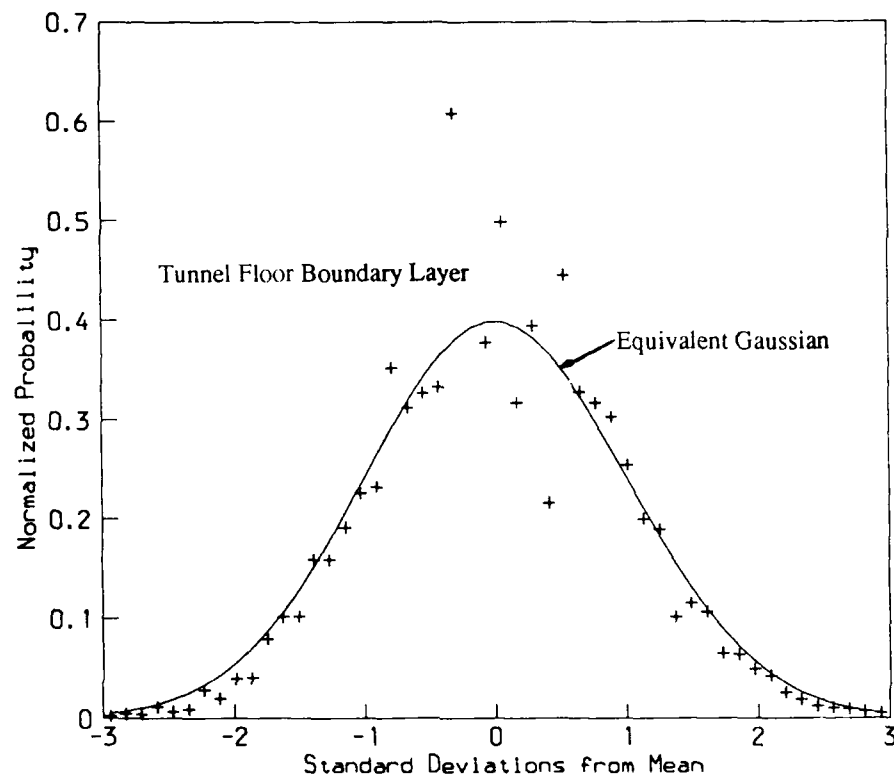


Figure 12 Probability Distribution of the P_w Fluctuation Amplitudes

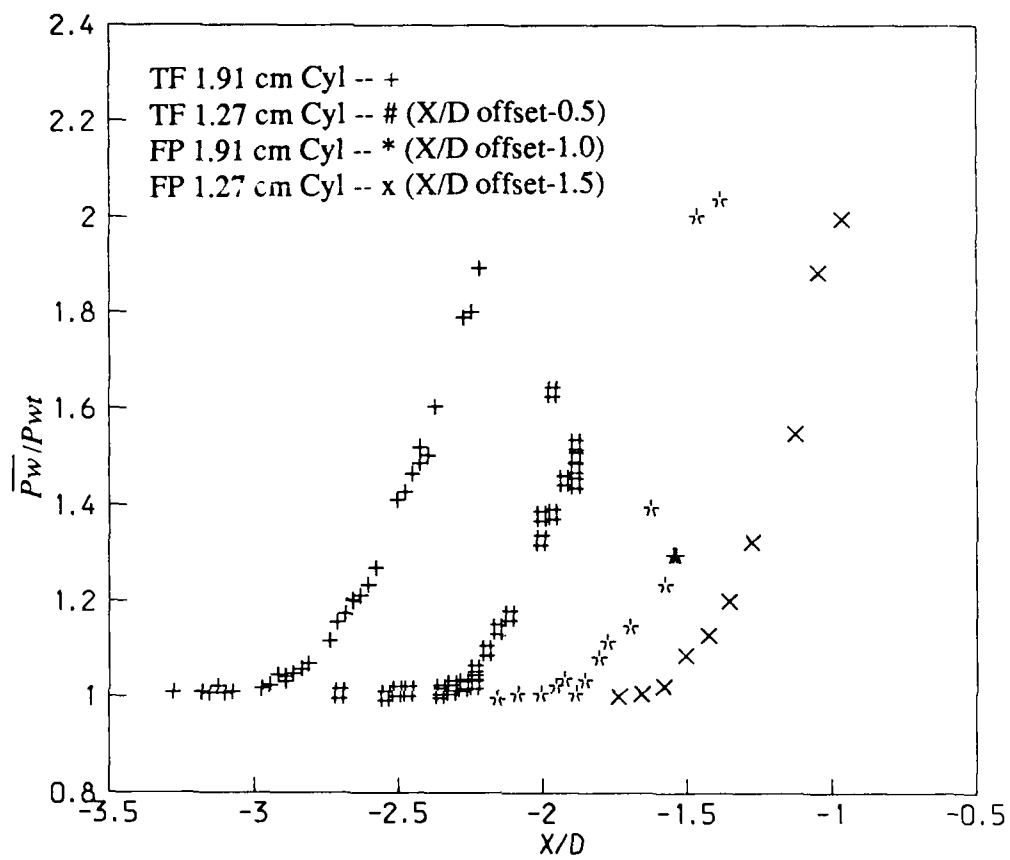


Figure 13 Streamwise Distribution of P_w

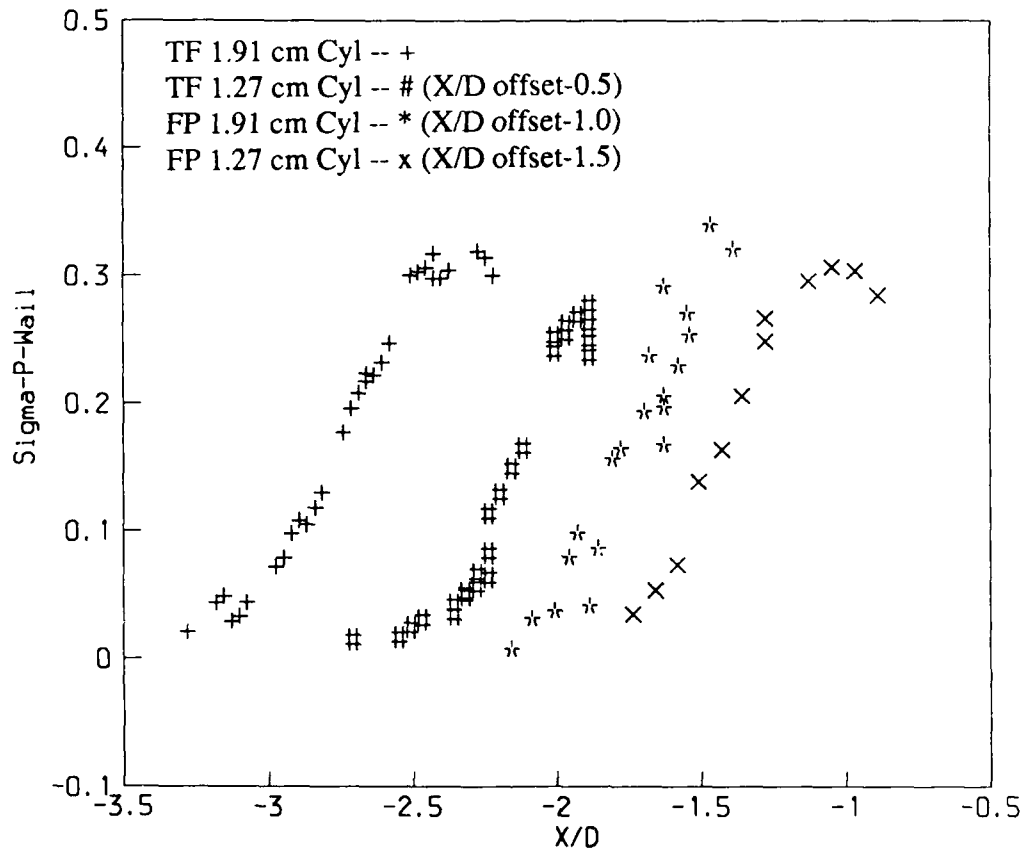


Figure 14 Streamwise Distribution of σ_{Pw}

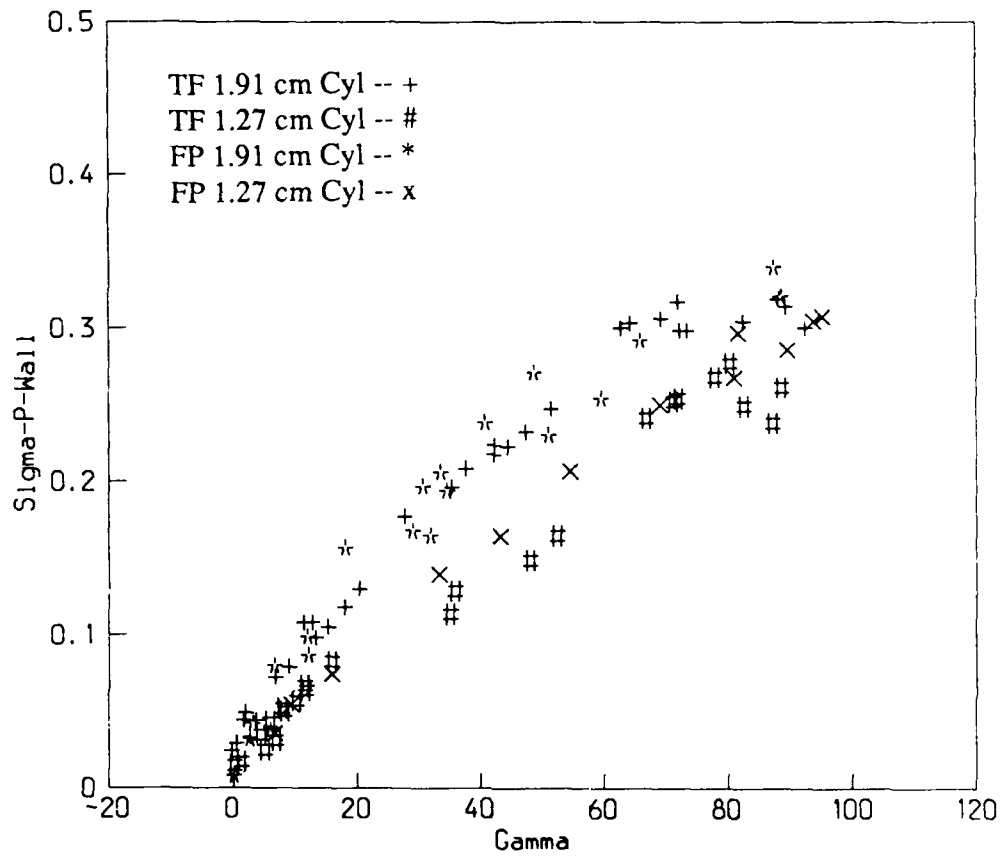


Figure 15 Distribution of σ_{P-W} Through Intermittent Region

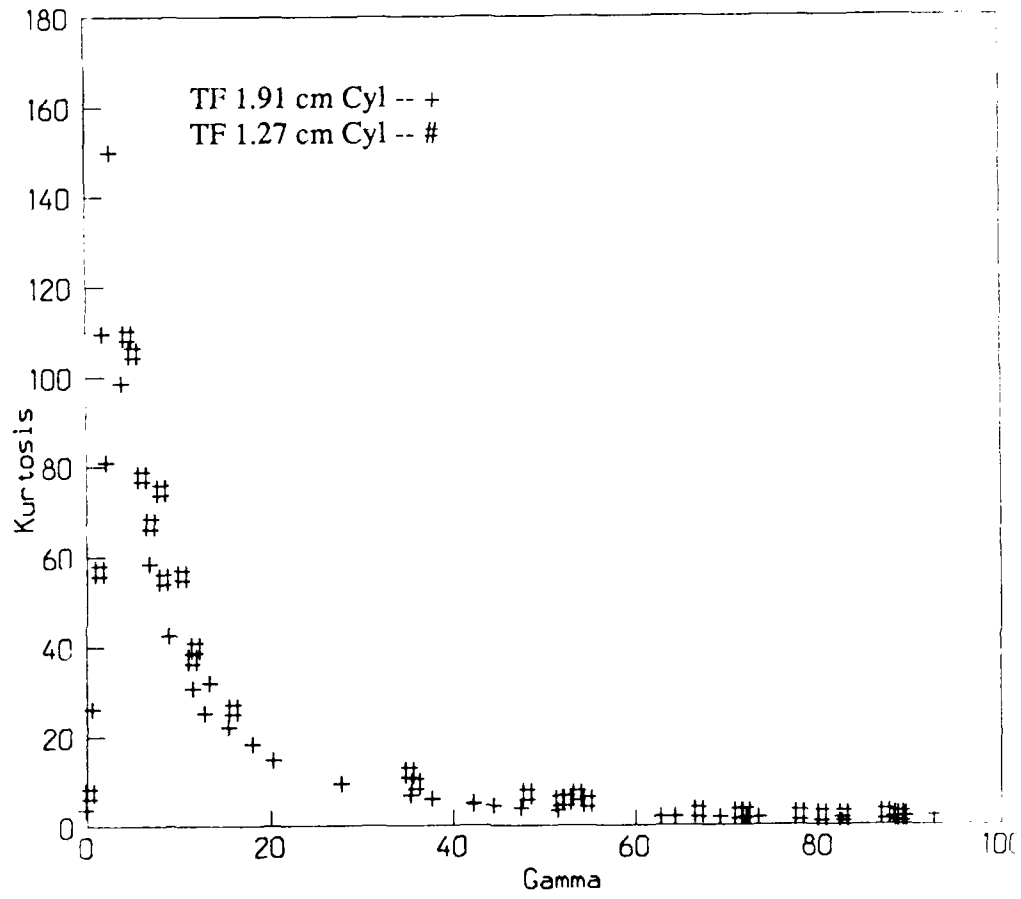


Figure 16 Streamwise Distribution of Flatness Coefficient

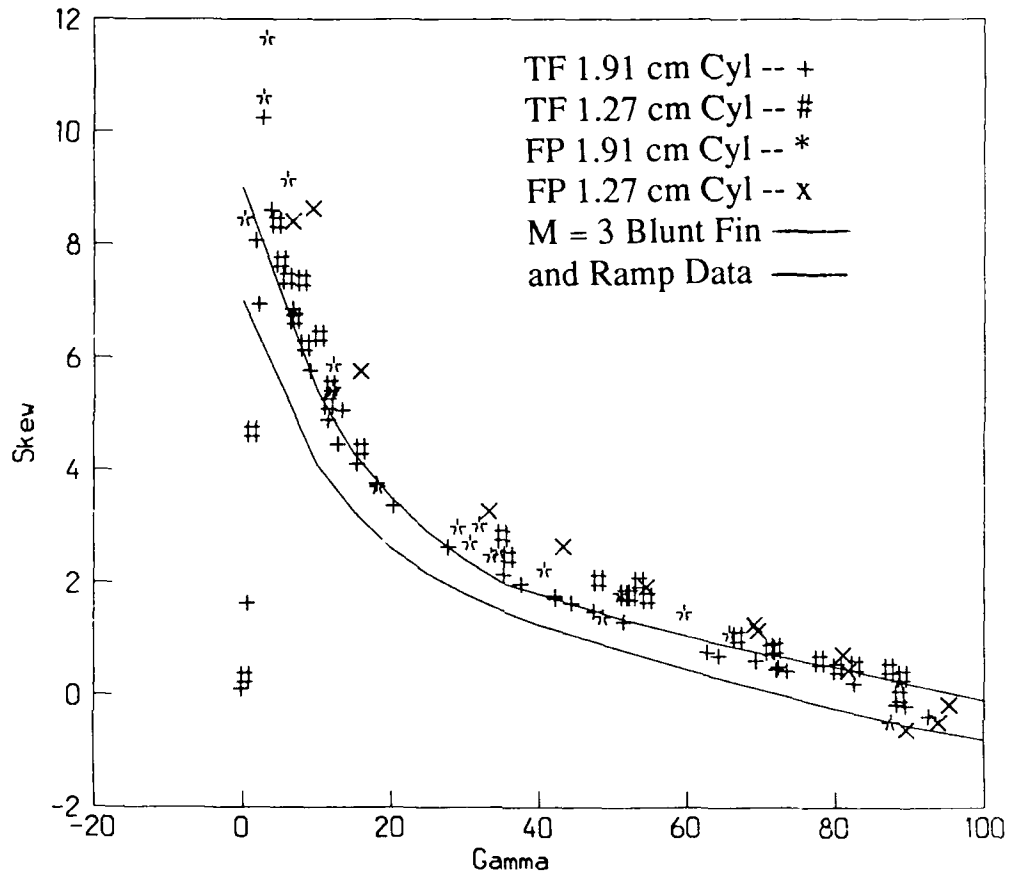


Figure 17 Streamwise Distribution of Skewness Coefficient

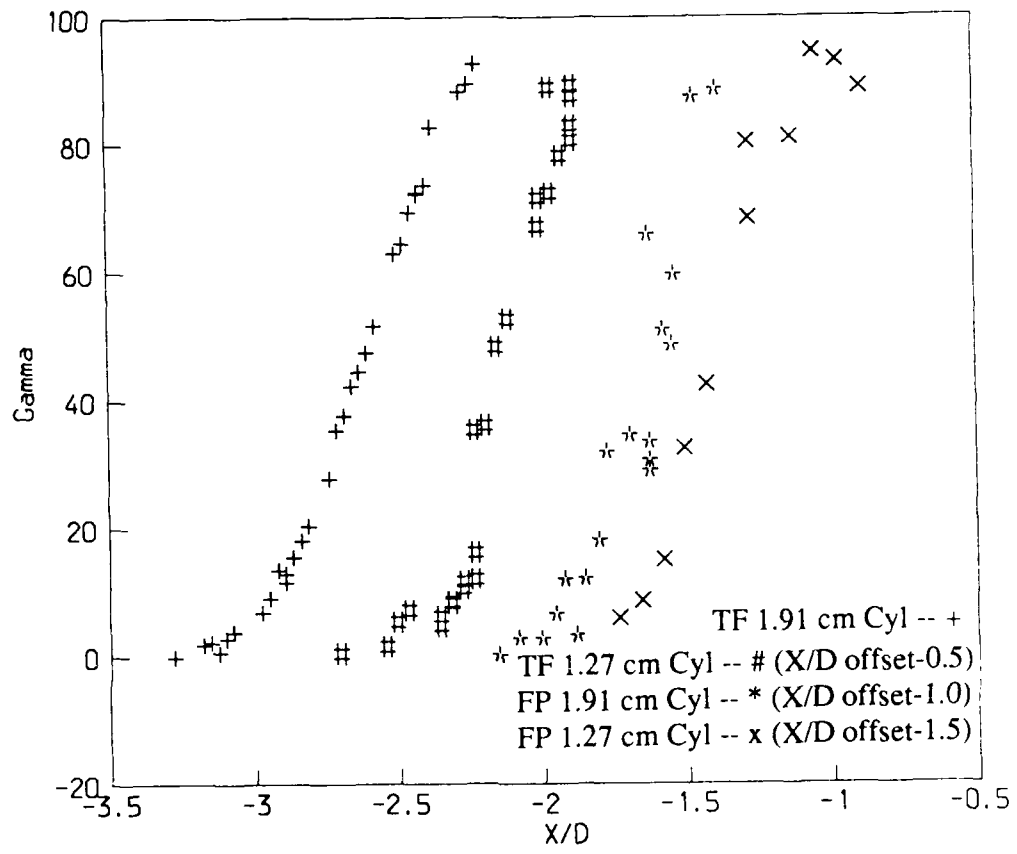


Figure 18 Streamwise Distribution of Intermittency

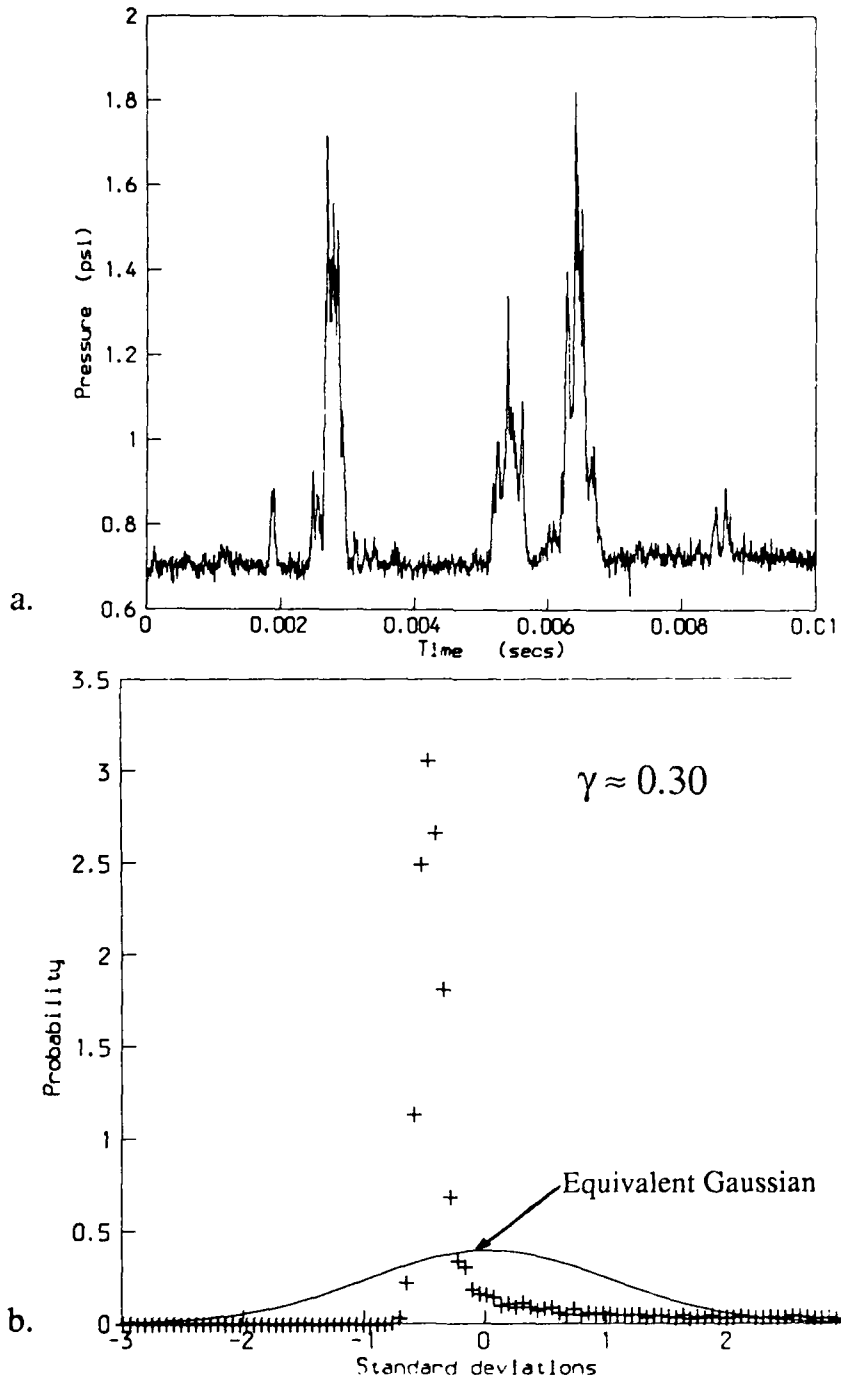


Figure 19 a. (top) Pressure-Time History, b. Probability Distribution of P_w Fluctuation Amplitudes

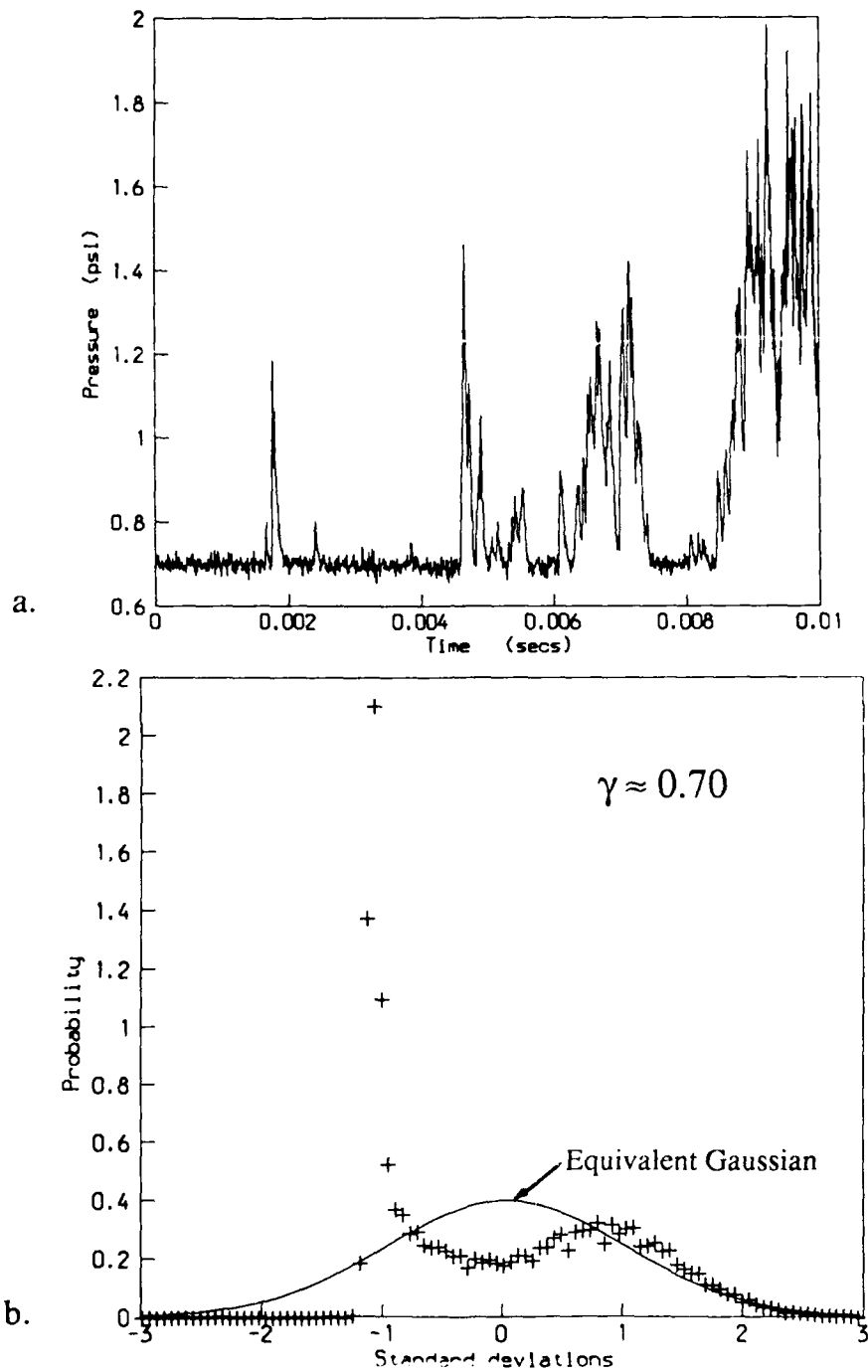


Figure 20 a. (top) Pressure-Time History, b. Probability Distribution of P_w Fluctuation Amplitudes

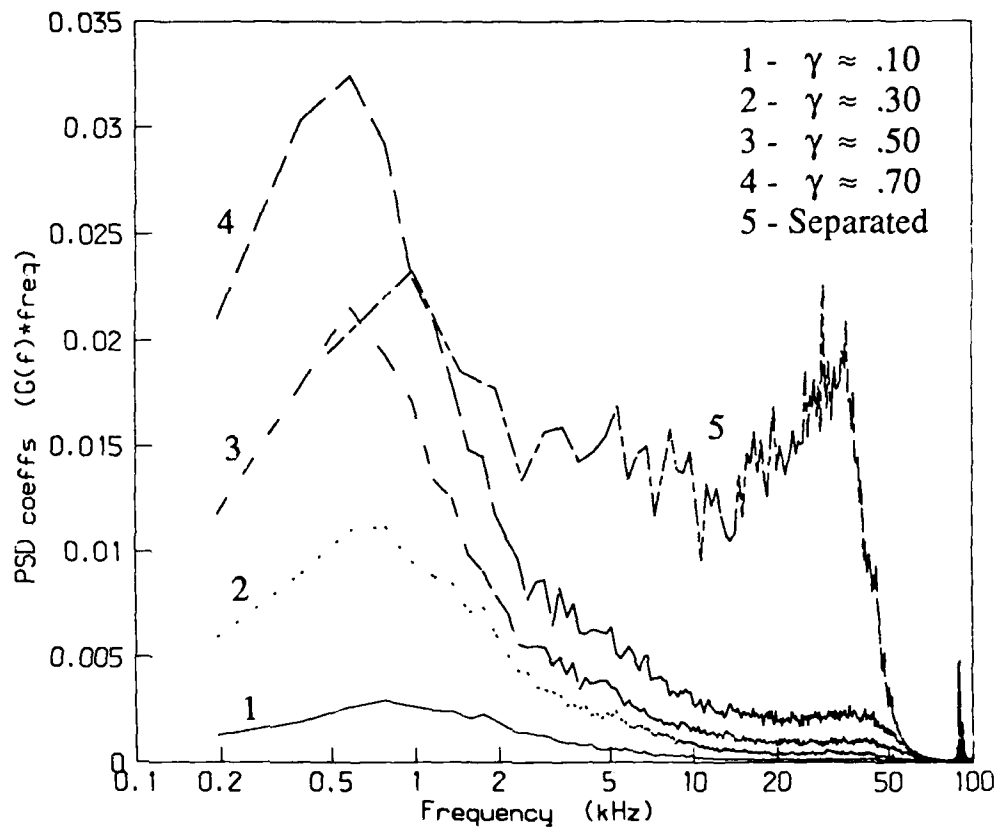


Figure 21 Dimensional Power Spectra of the P_w Fluctuation Amplitudes (TF, 1.91 cm Cyl)

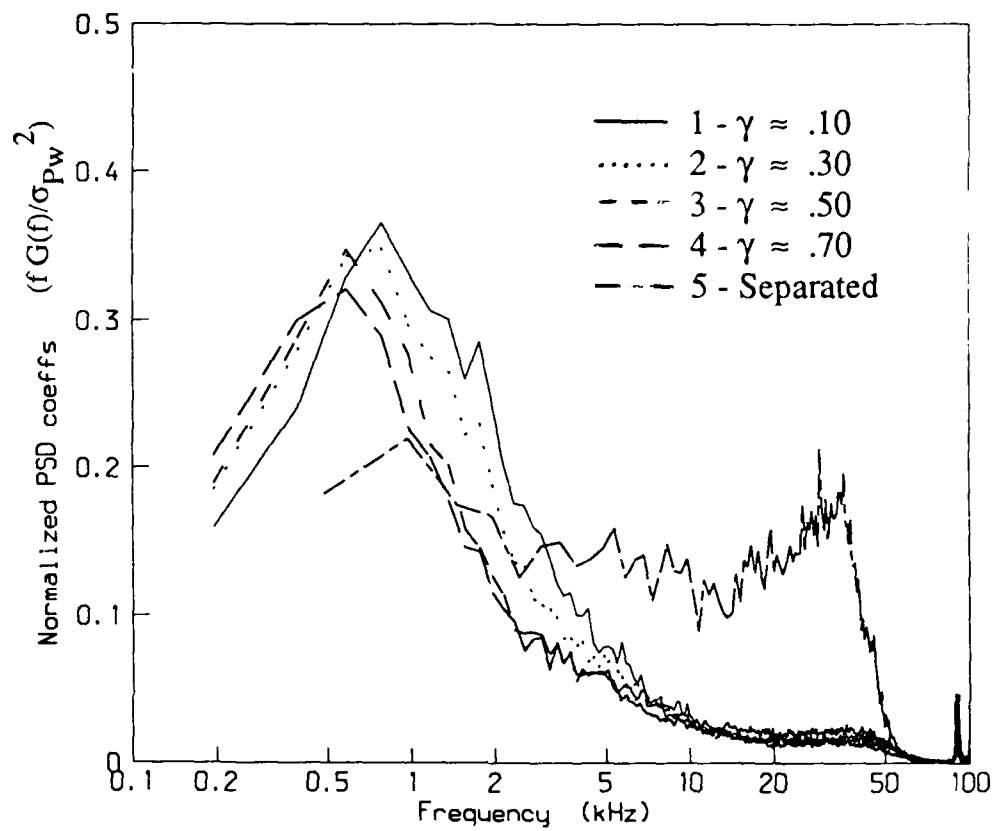


Figure 22 Normalized Power Spectra of the P_w Fluctuation Amplitudes (TF, 1.91 cm Cyl)

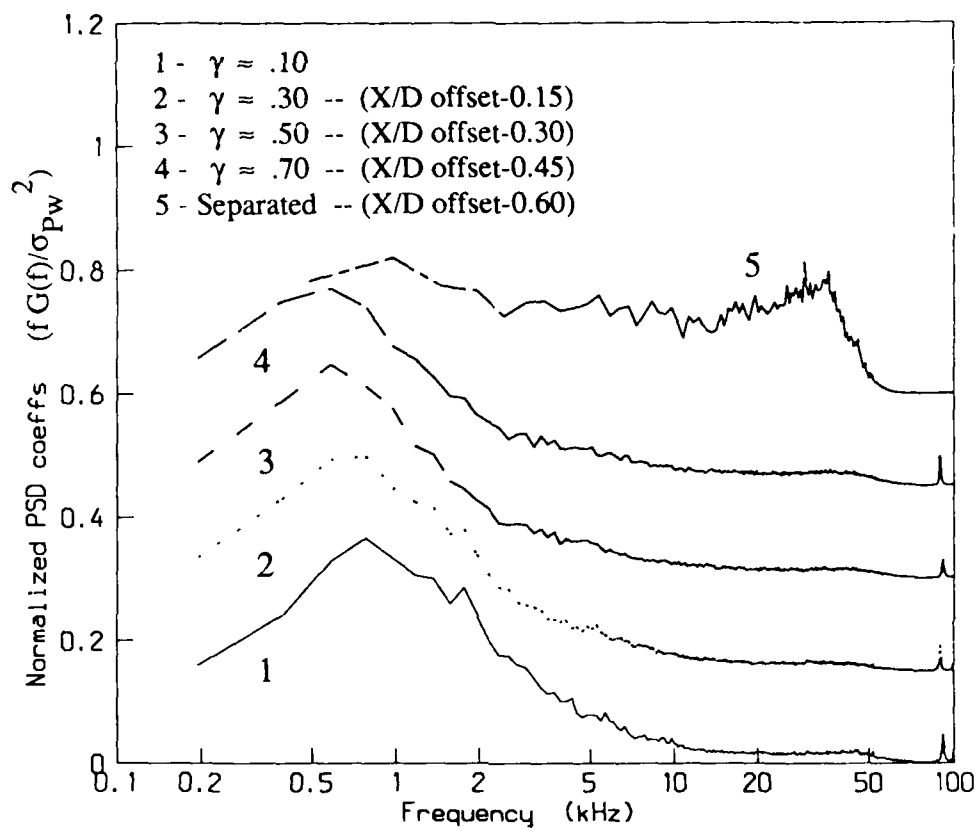


Figure 23 Normalized Power Spectra of the P_w Fluctuation Amplitudes (TF, 1.91 cm Cyl)

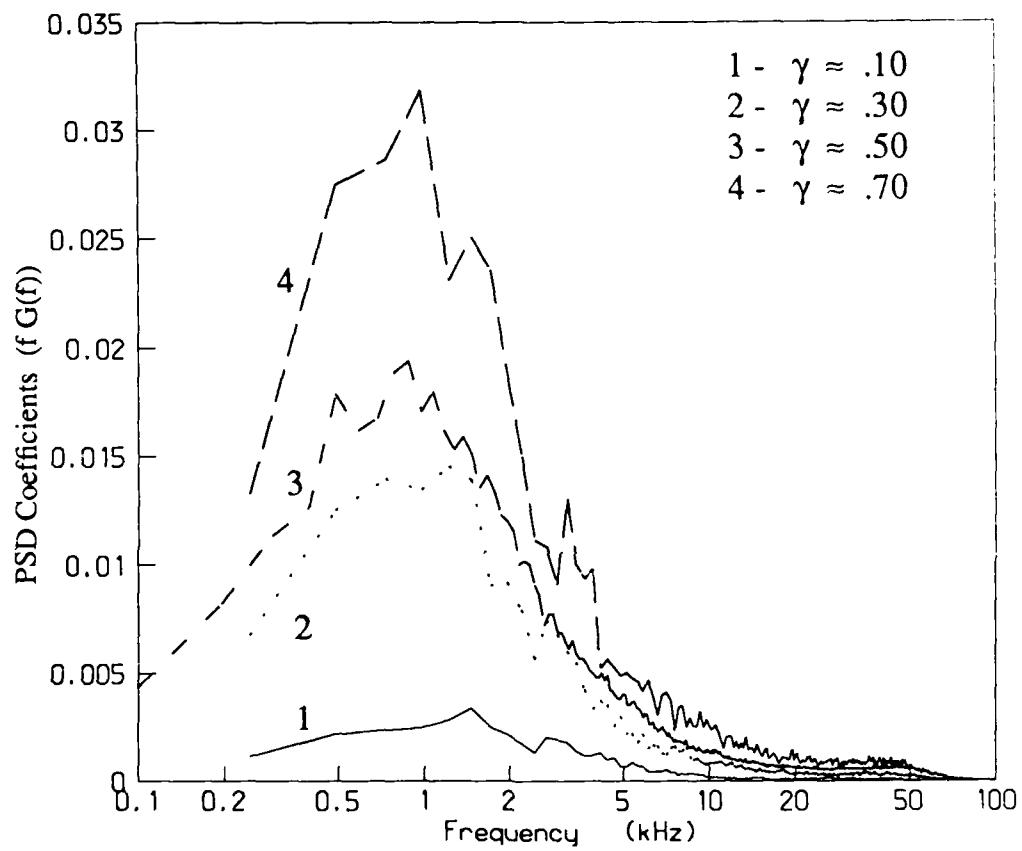


Figure 24 Dimensional Power Spectra of the P_w Fluctuation Amplitudes (FP, 1.91 cm Cyl)

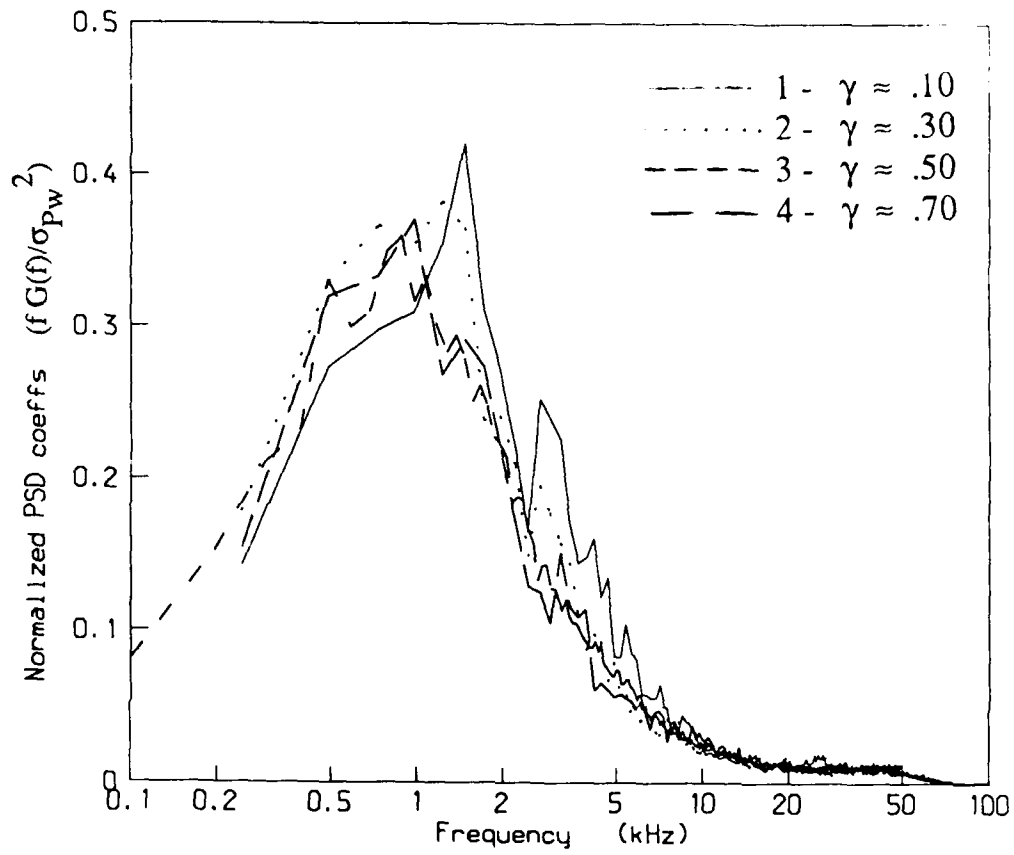


Figure 25 Normalized Power Spectra of the P_w Fluctuation Amplitudes (FP, 1.91 cm Cyl)

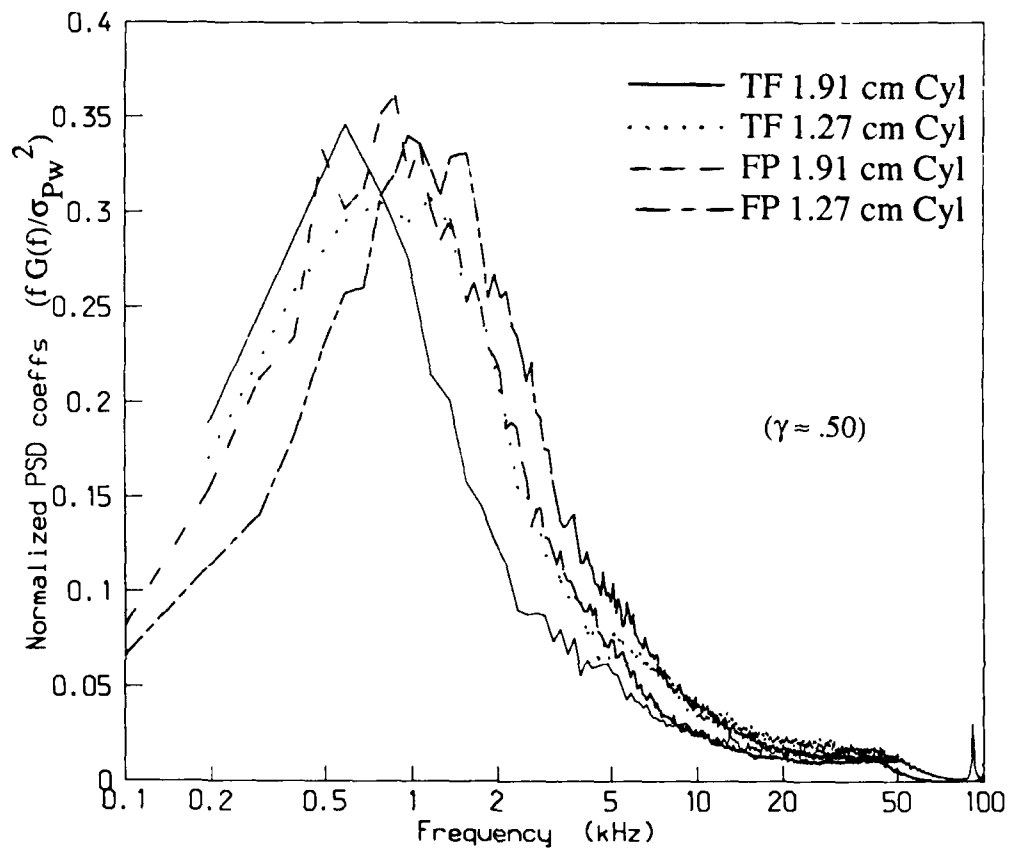


Figure 26 Normalized Power Spectra of the P_w Fluctuation Amplitudes

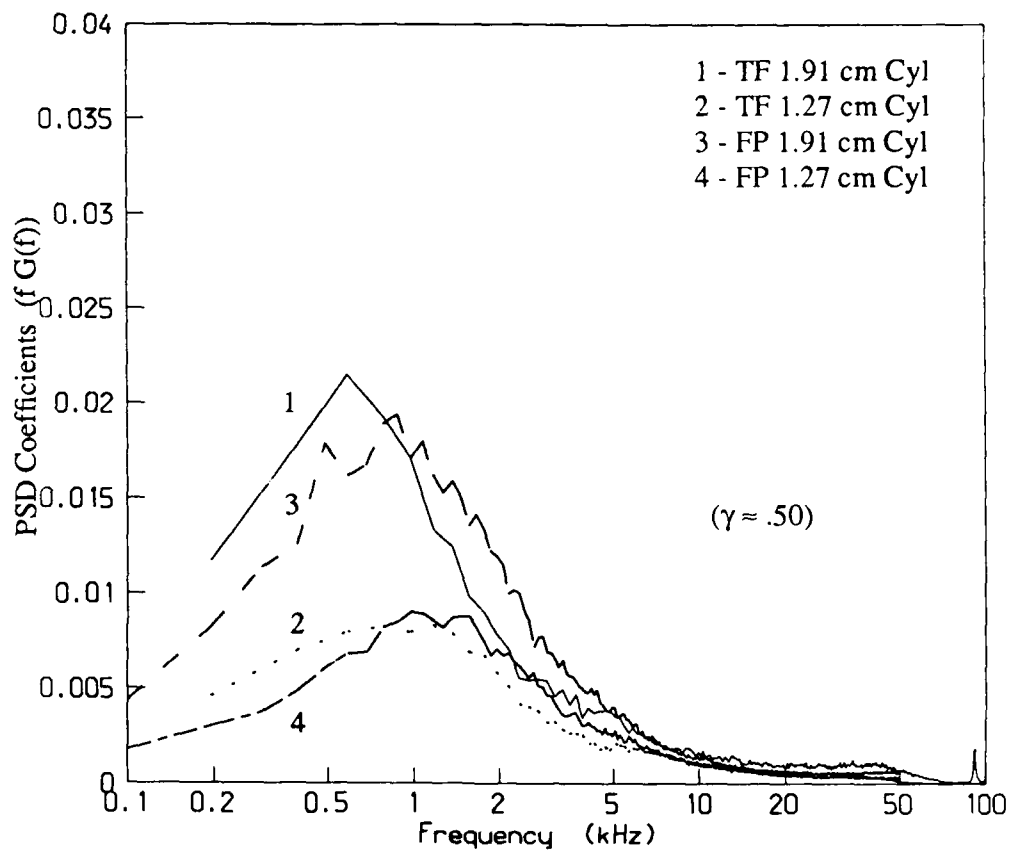


Figure 27 Dimensional Power Spectra of the P_w Fluctuation Amplitudes

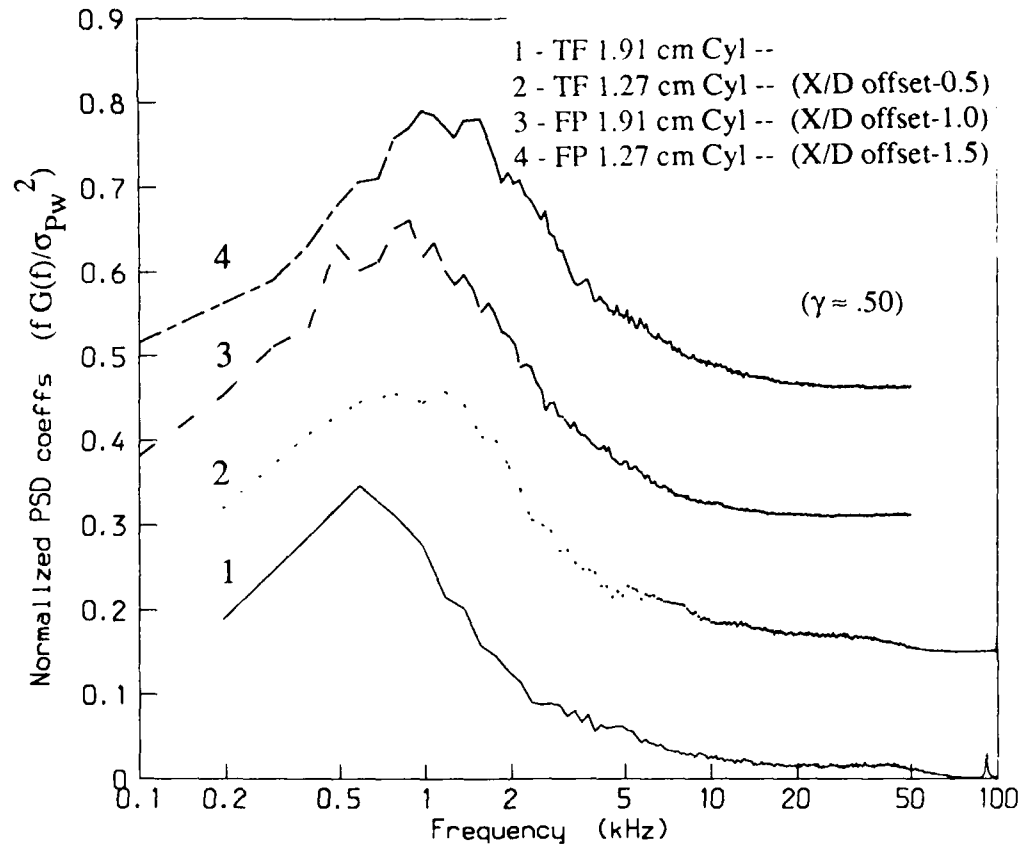


Figure 28 Normalized Power Spectra of the P_w Fluctuation Amplitudes

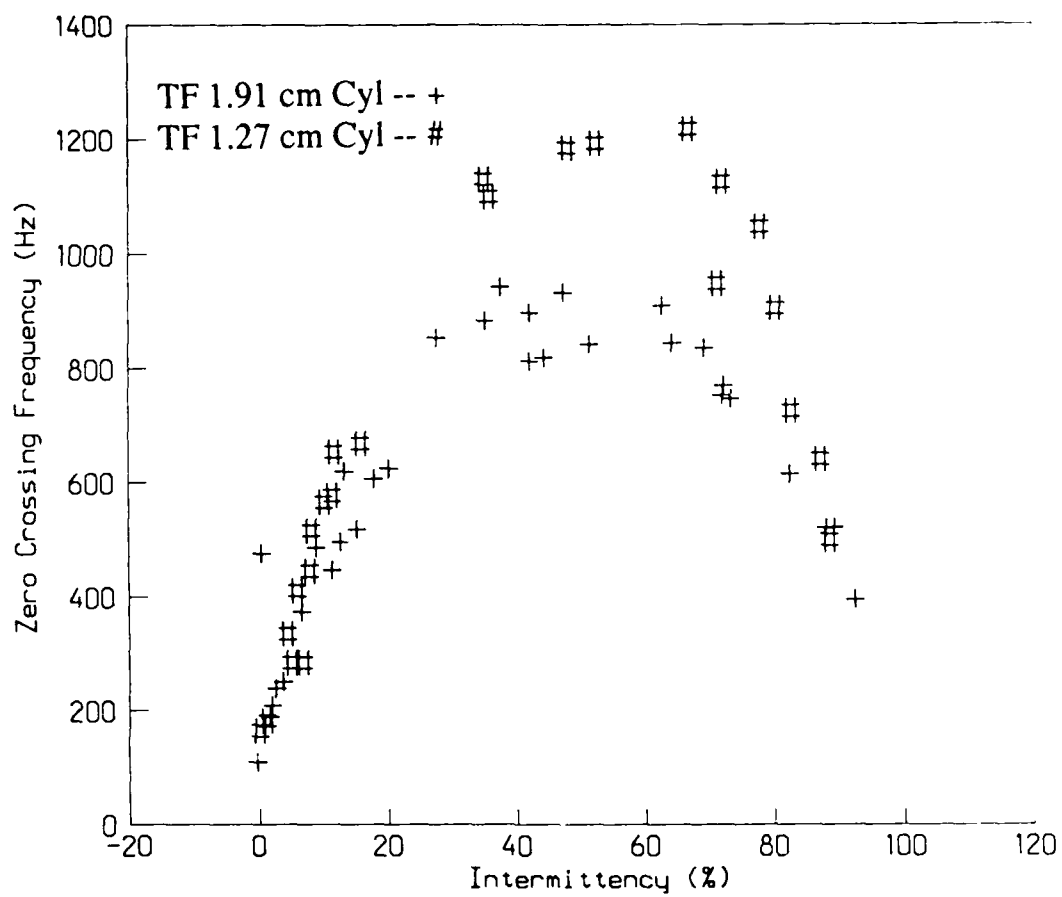


Figure 29 Plot of Zero Crossing Frequency versus Intermittency (TF only)

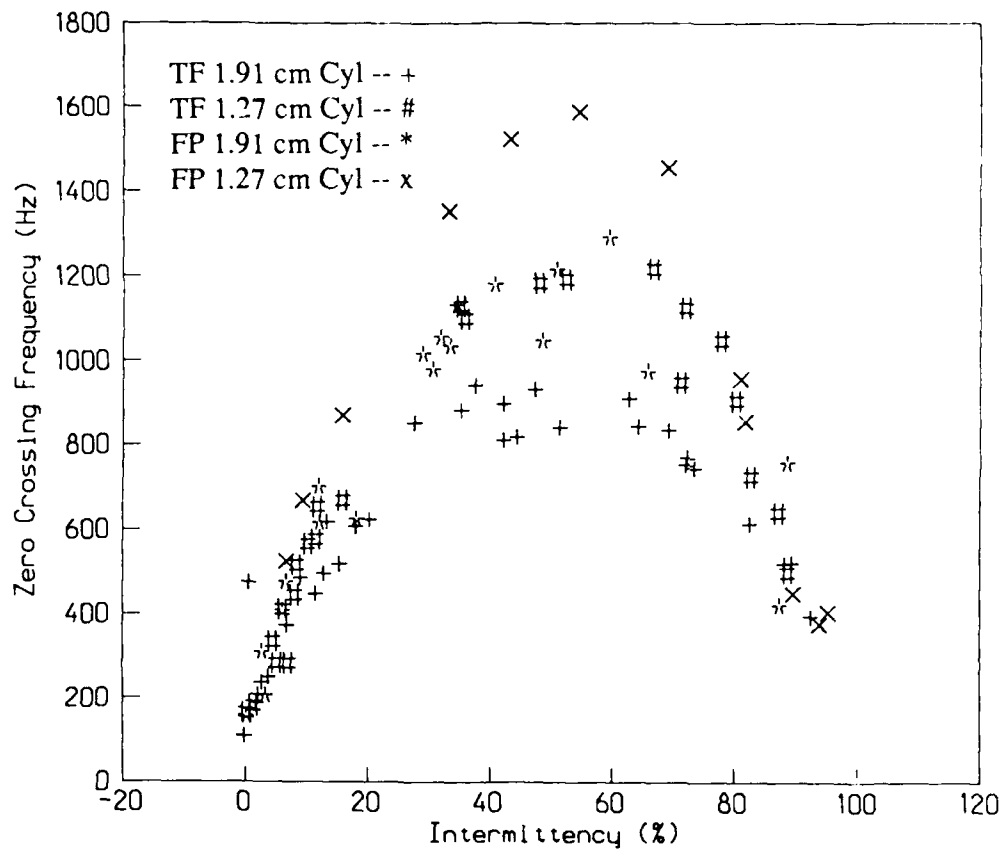


Figure 30 Plot of Zero Crossing Frequency versus Intermittency

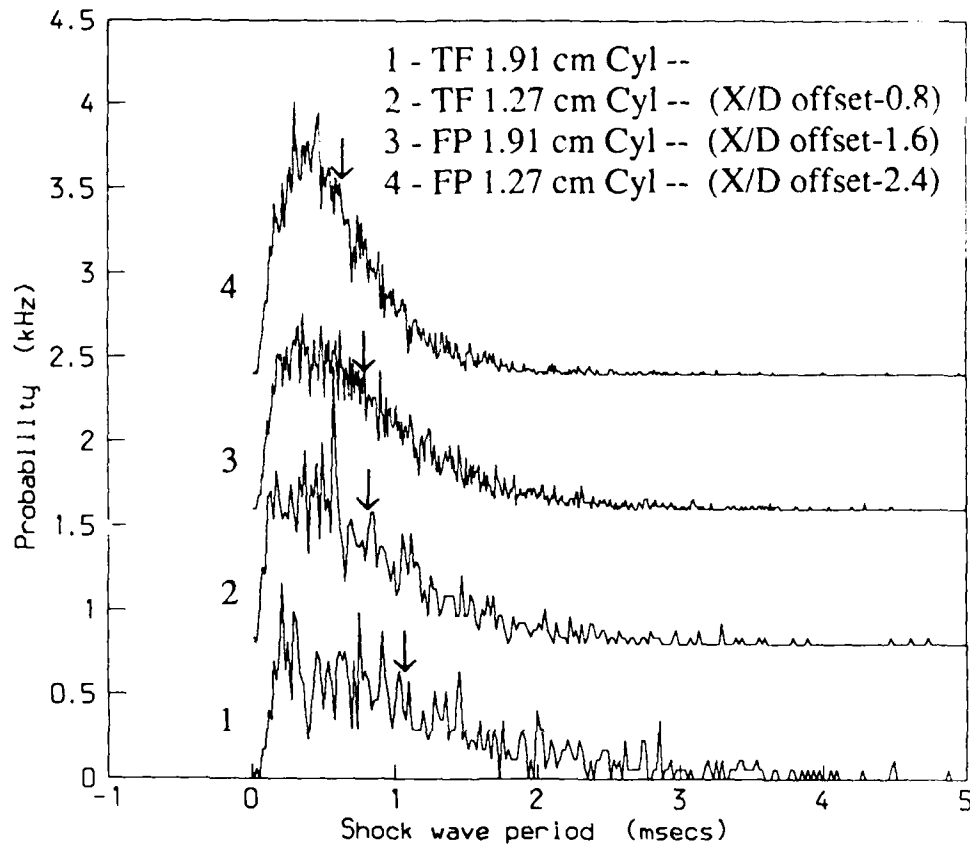


Figure 31 Probability Distribution of the Shock Periods

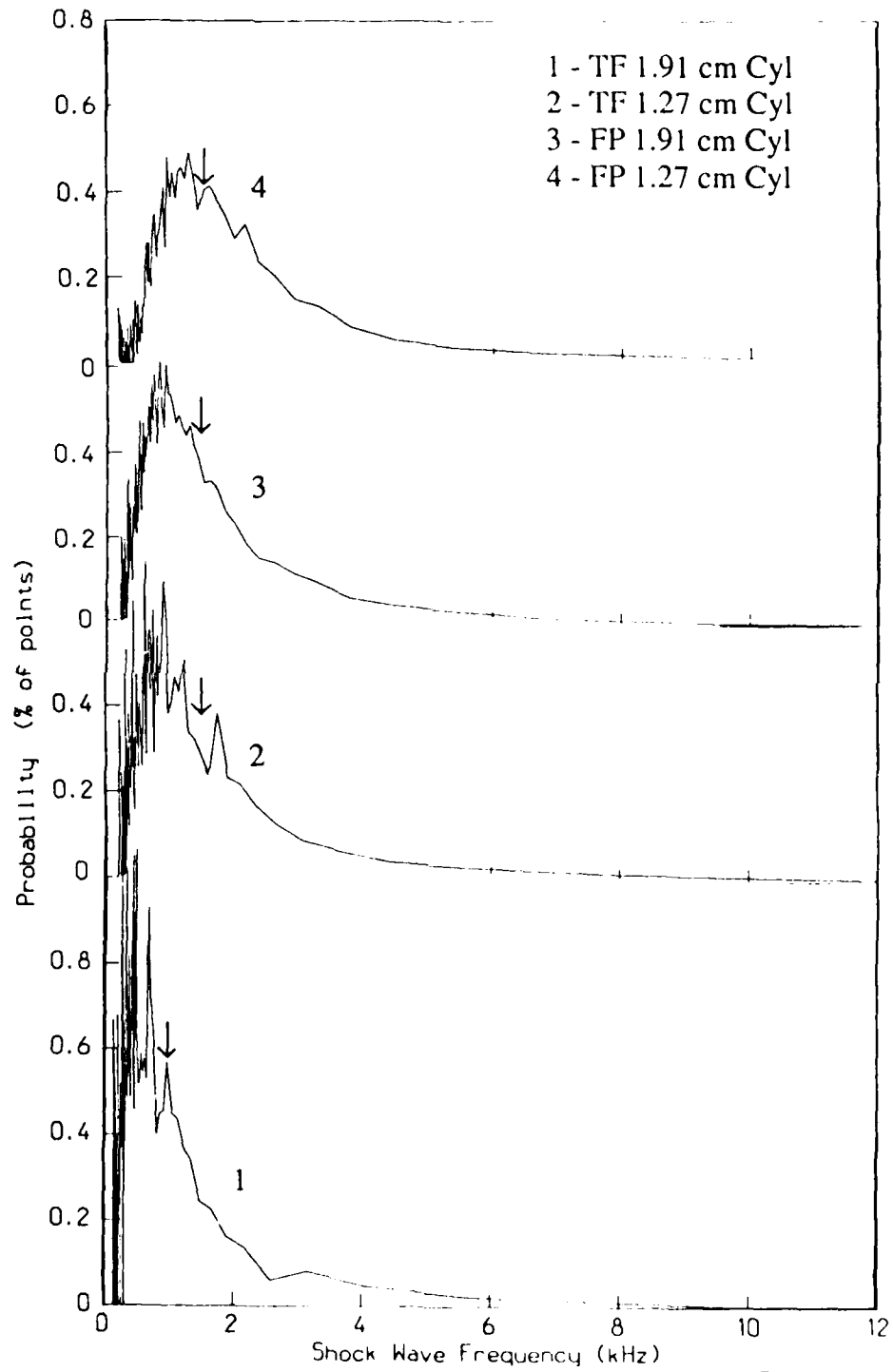


Figure 32 Probability Distribution of the Shock Frequency

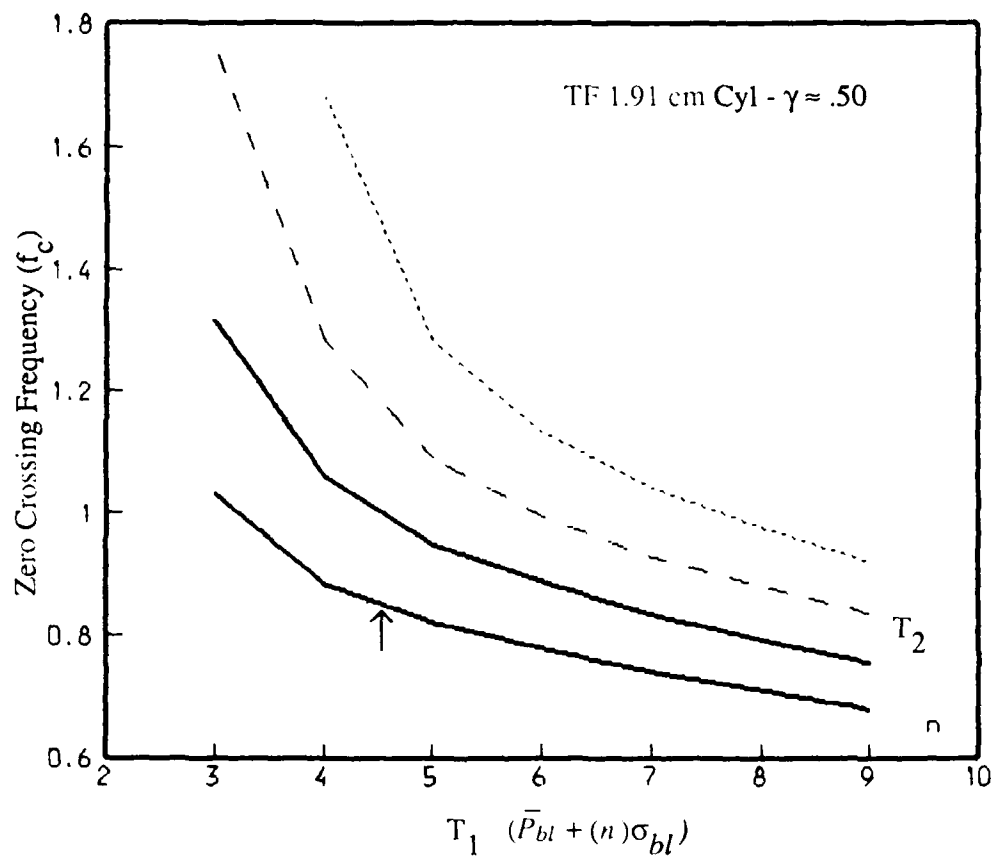


Figure 33 Variation of Zero Crossing Frequency with Threshold Settings

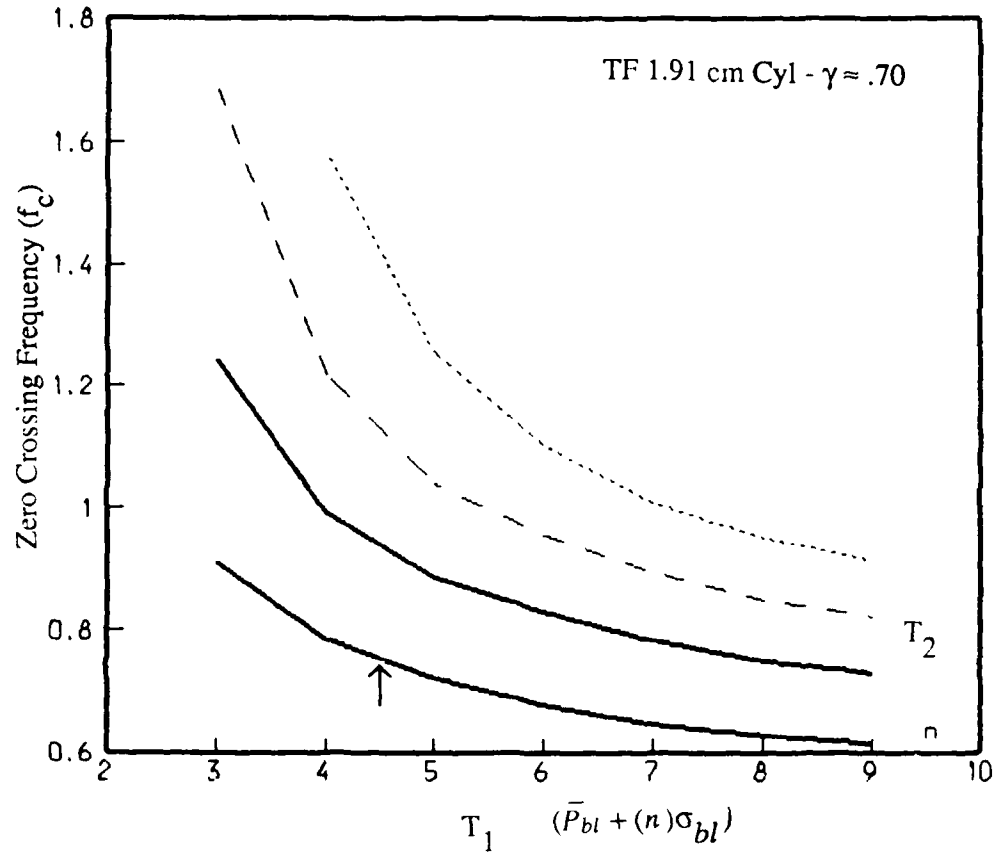


Figure 34 Variation of Zero Crossing Frequency with Threshold Settings

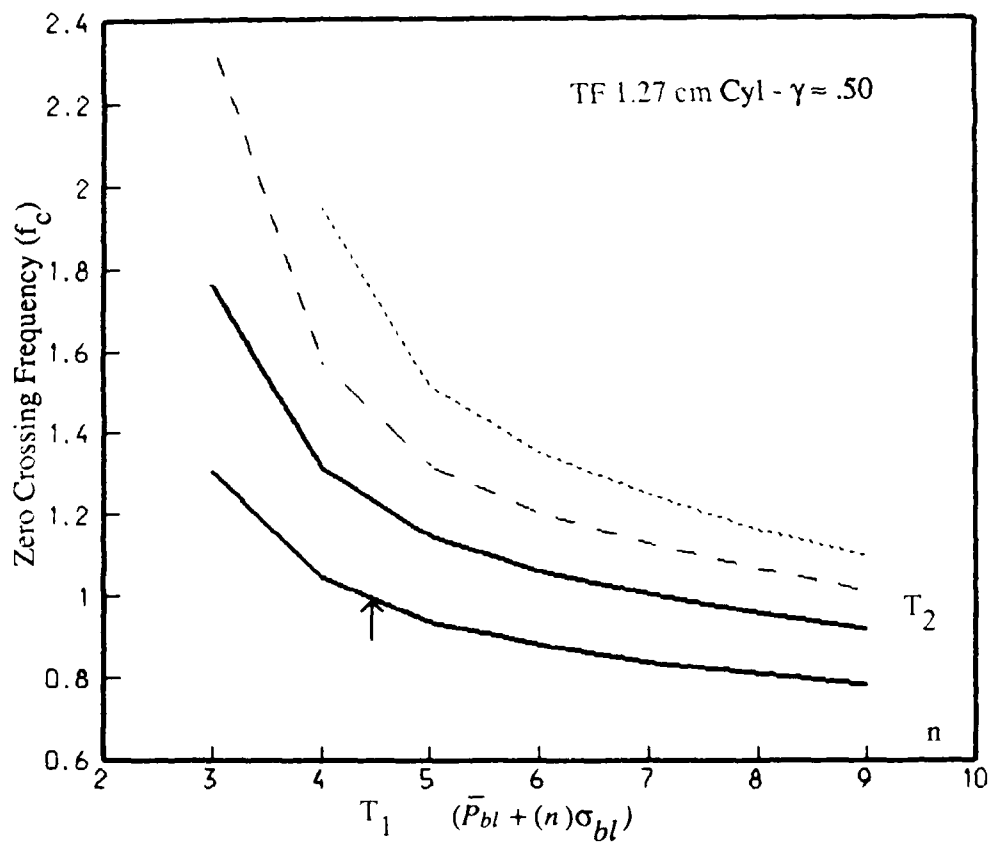


Figure 35 Variation of Zero Crossing Frequency with Threshold Settings

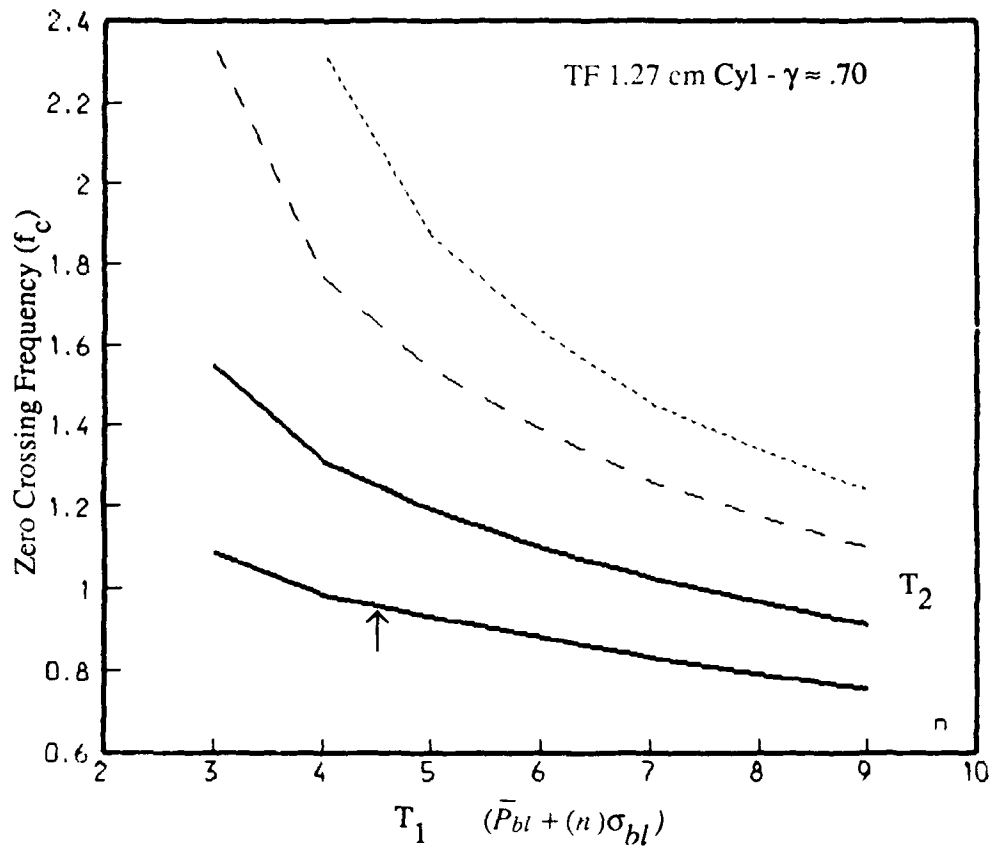


Figure 36 Variation of Zero Crossing Frequency with Threshold Settings

CHAPTER 7

REFERENCES

- [1] Bogdonoff, S. M. and C. E. Kepler, "Separation of a Supersonic Turbulent Boundary Layer," *Journal of Aeronautical Sciences*, Vol. 22, 1955, pp. 414-424.
- [2] Chapman, D. R., D. M. Kuehn, and H. K. Larson, "Investigation of Separated Flows in Supersonic and Subsonic Streams with Emphasis on the Effect of Transition," NACA TN 3869, March 1957, NACA TM 1356, 1958.
- [3] Kistler, A. L., "Fluctuating Wall Pressure Under Separated Supersonic Flow," *Journal of Acoustical Society of America*, Vol. 36, Mar 1964, pp. 543-550.
- [4] Dolling, D. S., "Unsteadiness of Shock-Wave-Induced Turbulent Boundary Layer Separation - A Review." IUTAM Symposium on Turbulent Shear Layer/Shock Interactions, Sept. 1985 (to be published Springer-Verlag).
- [5] Kaufman, L. G., R. H. Korkegi, L. C. Morton, "Shock Impingement Caused by Boundary Layer Separation Ahead of Blunt Fins," Aerospace Research Laboratories, ARL 72-0118, Aug 1972.
- [6] Young, F. L., L. G. Kaufman, R. H. Korkegi, "Experimental Investigation of Interactions Between Blunt Fin Shock Waves and Adjacent Boundary Layers at Mach Numbers 3 and 5," Aerospace Research Laboratories, ARL 68-0214, Dec 1968.
- [7] Price, E. A. and R. L. Stallings, "Investigation of Turbulent Separated Flows in the Vicinity of Fin-Type Protuberances at Supersonic Mach Numbers," NASA TN D-3804, February 1967.
- [8] Westkaemper, J. C., "Turbulent Boundary-Layer Separation Ahead of Cylinders," *AIAA Journal*, Vol.6, July 1968, pp. 1352-1355.
- [9] Sedney, R., and C. W. Kitchens, "Separation ahead of Protuberances in Supersonic Turbulent Boundary Layers," *AIAA Journal*, Vol.15, April 1977, pp. 546-552.

- [10] Dolling, D. S., and M. T. Murphy, "Unsteadiness of the Separation Shock Wave Structure in a Supersonic Compression Ramp Flowfield," *AIAA Journal*, Volume 21, December 1983, pp. 1628-1634.
- [11] Dolling, D. S., and C. T. Or, "Unsteadiness of the Shock Wave Structure in Attached and Separated Compression Ramp Flowfields," *Experiments in Fluids*, Vol. 3, 1985, pp.24-32.
- [12] Nordyke, R. J., "Experimental Investigation of Flow Field Three-Dimensionality of a Mach 5 Unswept Compression Ramp Interaction," MS Thesis, Dept. of Aerospace Engineering and Engineering Mechanics, University of Texas, Dec 1987.
- [13] Andreopoulos, J. and K. C. Muck, "Some New Aspects of the Shock Wave Boundary Layer Interaction in Compression Ramp Flows," AIAA Paper 86-0342, AIAA 24th Aerospace Sciences Meeting, Reno Nevada, Jan 1986.
- [14] Muck, K. C., J. P. Dussauge, and S. M. Bogdonoff, "Structure of the Wall Pressure Fluctuations in a Shock-Induced Separated Turbulent Flow," AIAA Paper 85-0179, Jan. 1985.
- [15] Muck, K. C., J. Andreopoulos, and J. P. Dussauge, "On the Unsteady Nature of Shock Wave/Turbulent Boundary Layer Interaction," Private Communication, Jun 1987.
- [16] Coe, C. F., W. J. Chyu, and J. B. Dods, "Pressure Fluctuations Underlying Attached and Separated Supersonic Turbulent Boundary Layers and Shock Waves," AIAA Paper 73-996, Oct 1973.
- [17] Tran, T. T., "An Experimental Investigation of Unsteadiness in Swept Shock Wave/Turbulent Boundary Layer Interactions," Ph.D. Dissertation, Mech. and Aero. Engineering Department, Princeton University, Oct 1986.
- [18] Dolling, D. S., C. D. Cosad, and S. M. Bogdonoff, "Three Dimensional Shock Wave Turbulent Boundary Layers Interactions - A Parametric Study of Blunt Fin-Induced Flows," AIAA Paper 78-159, Jan 1978.
- [19] Dolling, D. S., C. D. Cosad, and S. M. Bogdonoff, "An Examination of Blunt-Fin Induced Shock Wave Turbulent Boundary Layer Interactions," AIAA Paper 79-0068, Jan 1979.

- [20] Dolling, D. S. and S. M. Bogdonoff, "An Experimental Investigation of the Unsteady Behavior of Blunt Fin-Induced Shock Wave Turbulent Boundary Layer Interactions," AIAA Paper 81-1287, June 1981.
- [21] Dolling, D. S. and S. M. Bogdonoff, "Blunt Fin-Induced Shock Wave/Turbulent Boundary-Layer Interaction," *AIAA Journal*, Vol. 20, No. 12, December 1982, pp.1674-1680.
- [22] Dolling, D. S. , "Comparison of Sharp and Blunt Fin-Induced Shock Wave/Turbulent Boundary-Layer Interaction," *AIAA Journal*, Vol. 20, No. 10, October 1982
- [23] Gramann, R. A., "Development of a Technique for Detection of Unsteady Shock Induced Turbulent Boundary Layer Separation," MS Thesis, Dept. of Aerospace Engineering and Engineering Mechanics, University of Texas, May 1986.
- [24] Narlo, J. C., II, "Experimental Investigation of the Driving Mechanisms of Separation Shock Wave Motion in Interactive Flows," MS Thesis, Aerospace Engineering and Engineering Mechanics Department, The University of Texas at Austin, Dec 1986.
- [25] Dolling, D. S. and Narlo, J. C.,II, "Driving Mechanism of Unsteady separation Shock Motion in Hypersonic Interactive Flow," AGARD Conference on "Aerodynamics of Hypersonic Lifting Vehicles," April 1987. Proceedings to be published.
- [26] Dolling, D. S. and Brusniak L., "Separation Shock Motion in Fin, Cylinder, and Compression Ramp-Induced Turbulent Interactions," AIAA Paper 87-1368, June 1987.
- [27] Dolling, D. S., "Wind Tunnel Testing in University Facilities," Notes for Short Course on "Hypersonics", The University of Texas at Austin, Nov 1986.
- [28] Hung, C. M. and W. Kordulla, "A Time-Split Finite Volume Algorithm for Three Dimensional Flowfield Simulation," *AIAA Journal*, Vol. 22, November 1984, pp.1564-1572.
- [29] Hung, C. M. and P. G. Buning, "Simulation of Blunt Fin Induced Shock Wave and Turbulent Boundary Layer Interaction," *Journal of Fluid Mechanics*, Vol. 154, May 1985, pp. 163-185.

- [30] Baade H., and Y. Shau, "Turbulent Boundary Layer Velocity Profile Measurement in Compressible Flow," Report for ASE 382Q, Dept of Aerospace Engineering and Engineering Mechanics, The University of Texas at Austin, Dec 1986.
- [31] Dolling, D. S. and S. M. Bogdonoff, "Scaling of Interactions of Cylinders with Supersonic Turbulent Boundary Layers," *AIAA Journal*, Vol. 19, No. 5, May 1981, p. 655.
- [32] Schewe, G., "On the Structure and Resolution of Wall Pressure Fluctuations Associated with Turbulent Boundary Layer Flow," *Journal of Fluid Mechanics*, Vol. 134, 1984, pp. 311-328.
- [33] Hanly, R. D., "Effects of Transducer Flushness on Fluctuating Surface Pressure Measurements," AIAA 2nd Aero-Acoustics Conference, AIAA Paper 75-534, Mar 1975.
- [34] Raman, K. R., "A Study of Surface Pressure Fluctuations in Hypersonic Turbulent Boundary Layers," NASA CR-2386, Feb 1974.
- [35] Gramann, R. A., and D. S. Dolling, "Unsteady Separation in Shock Wave Turbulent Boundary Layer Interactions," AIAA Paper 86-1033, May 1986.
- [36] Baada, H., and D. S. Dolling, "Space Time Correlations of Separation Shock Induced Pressure Fluctuations in Turbulent Flow," Submitted to the *Journal of Fluid Mechanics*, August 1987.
- [37] Smith, D. R., and D. S. Dolling, "Unsteady Shock-Induced Turbulent Separation in Mach 5 Cylinder Interactions," to be submitted to AIAA 26th Aerospace Sciences Meeting, Jan 1987, copies available on request.

